2014

3D RECONSTRUCTION OF RyR1 AND STRUCTURAL VALIDATION UNDER DIFFERENT LEVELS OF NOISE

Joshua J. Lobo

3D RECONSTRUCTION OF RyR1 AND STRUCTURAL VALIDATION UNDER DEIFFERENT LEVELS OF NOISE

A thesis submitted in partial fulfillment of the requirements for the degree of Master of Science at Virginia Commonwealth University.

by

Joshua Jude Lobo

B.E., University of Pune, India

2011

Director: Dr. Montserrat Samso, PhD.

Assistant Professor, Department of Physiology and Biophysics

Virginia Commonwealth University

Richmond, Virginia

December, 2014

Acknowledgements

I would like to thank my advisor; Dr. Montserrat Samso for her constant support, guidance and insight which was imperative to the success of this project. I would also like to thank my committee members; Dr. Ding-Yu Fei and Dr. Rebecca Heise for their support. Lastly I would like to thank Dr. Vanessa Cabra for her support and guidance throughout my research.

I would also like to thank my parents William and Marina Lobo for their untiring support and belief in me. This would not be possible without them. Furthermore, I would like to thank my sister Dr. Rachael Lobo for helping me with my physiology doubts and bringing me to the realization that understanding the human body is never going to be a clearly defined and well-structured engineering problem. Lastly, I would like to thank all my friends for their support. My gratitude to Urjita who has been my support system throughout this journey filled with happy and not so pleasant days.

Table of Contents

List of Tables

List of Abbreviations

List of Figures

Abstract

3D RECONSTRUCTION OF RyR1 AND STRUCTURAL VALIDATION UNDER DIFFERENT LEVELS OF NOISE

Joshua Jude Lobo, B.E.

A thesis submitted in partial fulfillment of the requirements for the degree of Master of Science at Virginia Commonwealth University.

Virginia Commonwealth University, 2014

Director: Dr. Montserrat Samso, PhD Assistant Professor
Department of Physiology and Biophysics

Ryanodine receptors (RyR) are intracellular channels that are intricately involved in Ca^{2+} release. These channels large membrane proteins~2.26MDa in size.

In this multi-goal project firstly we successfully studied the gating mechanics of the RyR1 in the presence of Mg^{2+}. We used single particle reconstruction and image processing techniques to obtain the 3D structure of the RyR1 with Mg^{2+}. The 3D structure in the presence of Mg^{2+} and an ATP analog is the closest representation of human physiological conditions. The open and closed state structures of RyR1 are known. However, the physiologically closed state has not been studied before. Understanding this structure will help in the understanding of protein interactions.

Our second goal was the validation of this 3D structure under different levels of noise. Validation under different noise levels analyzed the problem of noise bias is present in the field of cryo-EM and single particle reconstruction in select cases.

1. Introduction

1.1 Ryanodine Receptor (RyR)

Ryanodine receptors (RyR) are non-selective cation channels that release $Ca^{2+}$from the sarco-endoplasmic reticulum of excitable cells and non-excitable cells. The ion channel is a tetramer with each subunit containing approximately 5000 amino acids. In all therefore a single channel weighs around 2 M Da.The portion of the RyR that forms the ion pore is located at the carboxy terminus and represents about 10 % of the total protein. In mammals there are three different genes encoding for the various isoforms RyR (RyR1, RyR2, RyR3).RyR1 is abundantly expressed in skeletal muscle, more specifically speaking in fast twitch muscle. The RyR2 isoform is expressed in abundance in the heart.RyR3 was identified as an inducible protein in lung epithelial cells but is widely expressed .RyR1 and RyR2 play a central role in excitation-contraction coupling of striated muscles. RyRs are large ion pores with an estimated unitary current of 0.5pA under quasi-physiological conditions [3].

1.2 Excitation Contraction Coupling in Skeletal Muscle

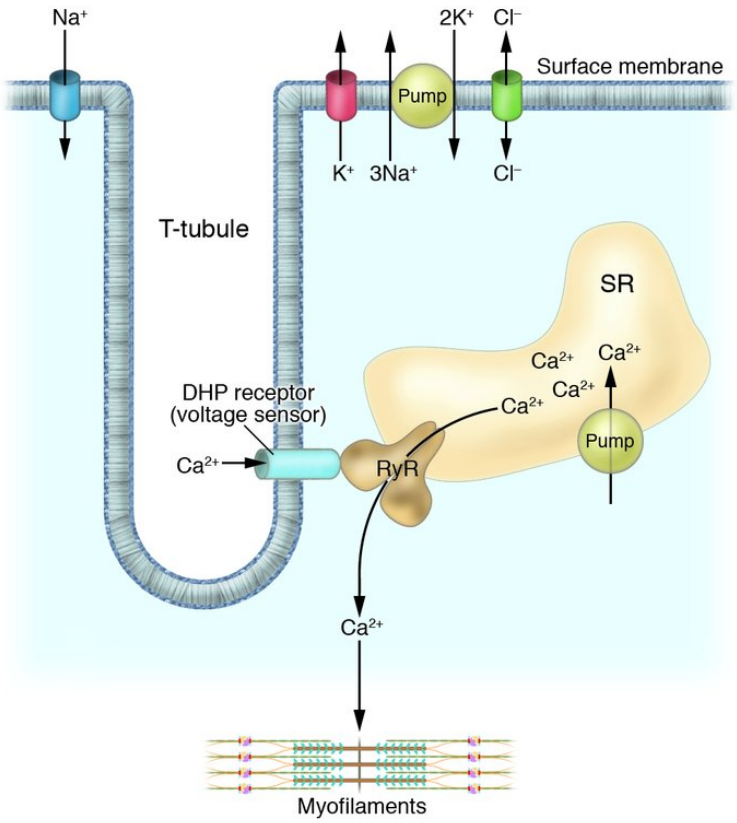

Figure.1:Excitation Contraction Coupling in Skeletal Muscle

A muscle fiber is excited by an action potential delivered by a nerve. This action potential then spreads out along the surface membrane entering the muscle through the transverse tubular system. The dihydropyridine (DHP) receptor senses the membrane depolarization

and alters its conformation. This activates the ryanodine receptor, which releases Ca^{2+} from the SR which is a Ca^{2+} store. The released Ca^{2+} binds to troponin and activates the contractile machinery [4].

It is already a well-established fact that the excitation-contraction process in the case of skeletal muscle majorly involves the physical interaction between the skeletal isoforms of dihydropyridine receptor L-type Ca^{2+} channel (DHPR) and ryanodine receptor Ca^{2+} release channel (RyR1). A signal is known to originate from the α_{1S} subunit of the DHPR L-type Ca^{2+} channel. The message is then transmitted further to the cytoplasmic domain of RyR1.This is followed by a protein gating mechanism which opens the RyR1 pore to allow the flow of Ca^{2+} into the cytoplasm. Once the Ca^{2+} is in the cytoplasm it activates the contractile machinery.

There are several factors to take into consideration when talking about EC coupling particular to skeletal muscle the first factor being membrane geometry. This geometrical aspect is clearly visible in the above figure which shows the transverse (t-) tubules of the plasma membrane come into close association with the membranes of the sarcoplasmic reticulum (SR) Ca^{2+} store. There are the regions where functional coupling takes place. The “junctional” gap between the surface and the SR membranes is approximately 10 nm wide. This narrow width facilitates membrane protein interaction. In adult skeletal muscle “triads” form .Triads are consisted of a t-tubule that is surrounded by terminal expansions of the SR on either side. [5]. These terminal expansions are also called as terminal cisterna.

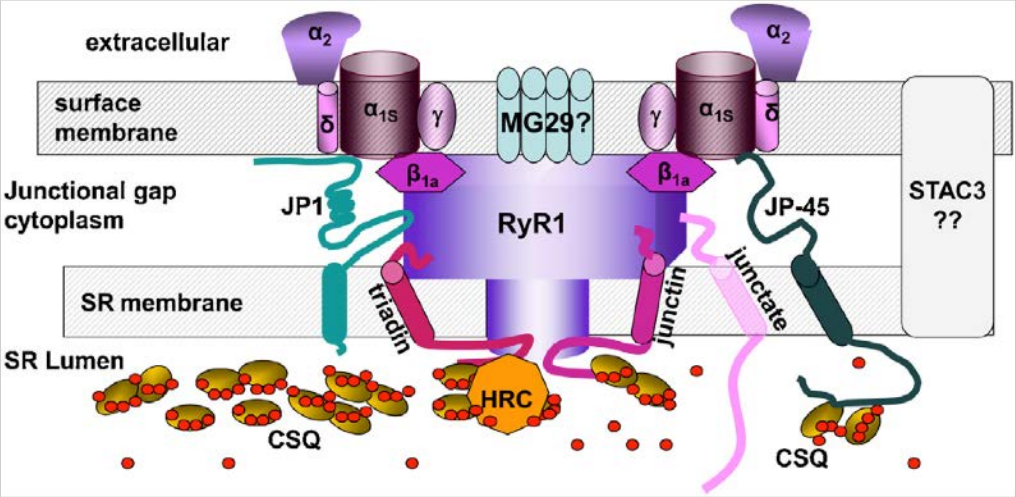

Figure 2:Diagramatic representation of a triad junction

Components of the triad junction and "couplon" RyR1 complex. Two subunits of RyR1 are shown, each with their associated DHPR consisting of 5 subunits of which α_{1S} binds to and β1a binds to RyR1 [5].

The above figure shows the three proteins that are essential in E-C coupling. Particularly the $\alpha_{1s,}$ β_{1a} and the RyR. Knockout of any one of the proteins leads to embryonic death hence exhibiting their vitality to the E-C coupling process. The α_{1S} subunit acts as a voltage sensor and responds to depolarization that is brought about by an action potential. A unique property of the coupling between DHPR and RyR1 is a bi-directional signaling mechanism. "Retrograde" coupling is a process in which the RyR dictates the characteristics of the L-type

Ca^{2+} channel [6]. The retrograde influence is on the α_{1S} which in turn enhances the Ca^{2+} flow across the surface of t-tubule membrane [5, 7]. “Orthograde coupling” on the other hand is the process according to which a signal passes from the DHPR to the RyR1.The uniqueness of this coupling lies in the fact that it doesn’t need a Ca^{2+} current through the DHPR which also makes it very unlike the E-C coupling process in the heart which involves the RyR2 isoform. The fact that E-C coupling in skeletal muscle is independent of a Ca^{2+}signal has led to the formation of the “conformational hypothesis” [6, 8]. There is very strong structural evidence in favor of the conformational hypothesis. The method of freeze fracture electron microscopy is used to obtain views which then work to provide insight into the macromolecular architecture of membranes. This method thereby provides information purely pertaining number as well as the distribution of transmembrane molecules [9]. To corroborate with the conformational hypothesis mutation studies that were carried out with either of the essential proteins (α_{1S}, β_{1a} subunits of DHPR and RyR1) knocked off produced a disrupted tetrad structure. The tetrad structure is essentially 4 DHPR‘s arranged in correspondence to 4 binding sites on an RyR1 cytoplasmic domain. Furthermore, manipulations that restored the tetrad formation also led towards the restoration of E-C coupling [5, 10-13].

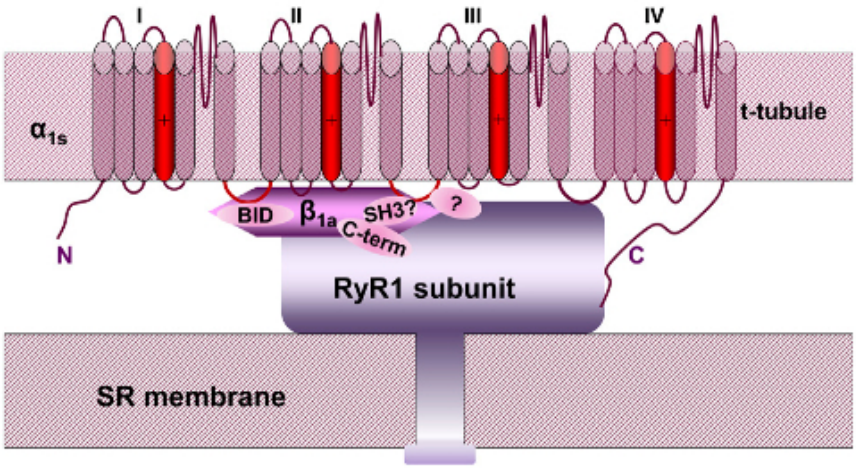

Figure 3: DHPR Triadic Junction

The α_{1s} and β_{1a} subunits of the DHPR and their likely interactions with one subunit of RyR1. The α_{1s} subunit contains four membrane spanning repeats each containing six transmembrane helices in addition to a "pore loop". Helices 5 and 6 line the pore, while helix 4 contains positively charged residues which allow it to "sense" the voltage across membrane and to respond to changes in voltage. The four repeats are connected by cytoplasmic loops for which some specific functions have been identified. The β subunit contains a binding site for the I–II loop known as the beta interaction domain (BID). In skeletal muscle, the II–III loop of the α_{1S} isoform contains sequences that are specific for the retrograde and orthograde interactions in skeletal EC coupling and for targeting the DHPRs into a tetrad formation which allows interactions between the DHPR and RyR. The III–IV loop also interacts with the RyR. Mutations in this loop lead to a malignant hyperthermia (MH) phenotype in which RyR1 is hypersensitive to activating stimuli [14]. Finally the C-terminal tail of the α_{1S} subunit interacts with RyR1 [15].

The α_{1S} of the DHPR is coded by 4 genes. As mentioned earlier it is a canonical voltage gated ion channel. The structure shown above in Fig.3 consists of four membrane inserted repeats .Each of the repeats contain six transmembrane domains out of which the fourth (S4) contains

a number of positively charged residues which align with the membrane field and hence facilitate the voltage sensing function of the subunit .The α_{1S} subunit contains critical sequences that are found in the central II-III loop. This region however is unstructured [16] and thus is in agreement of the hypothesis which suggests that it goes through a rapid conformational change following the movement of charge through the subunit. [5].Structural studies, also confirmed the conformational coupling hypothesis. In these studies RyR1 was treated with ryanodine which lead to structural changes which in turn altered the arrangement of the DHPR tetrads [17]. A 2nm shift in spacing of the α_{1S} subunit proved that the α_{1S}-RyR1 complex acted as a unit [5].

1.2.1 Beta Subunit of DHPR receptor.

Figure 4:Schematic of Beta subunit of DHPR

Schematic domain modules of Ca^{2+}-channel subunits. The SH3 and guanylatekinase (GK) domains are conserved in all subunits with the greatest sequence variability observed in the N, C termini and the hook region [18]

The other important subunit, shown in Fig 3 is the β subunit which belongs to a family of membrane associated guanylate kinases (MAGUK) structural proteins. The β subunit is unique because it is located entirely in the cytoplasm [18]. In Fig.4 we see the general structure of a β domain containing 5 domains. X ray crystallographic studies and homology modelling have shown that the Src homology (SH3) domain as well as the Guanylate-kinase-like domain (GK) remains highly conserved among the different isoforms [19-21] and are also referred to as the "core" domain[18].Despite of the GK subunit being enzymatically inactive (ATP binding motif is absent[22]) it still forms a very stable core by the interaction with the SH3 domain.

The β subunit interacts with the α1 subunit with a high affinity. This interaction basically takes place between the alpha interaction domain (AID) in the α1 subunit and the β subunit. The binding affinity of the β subunit for the AID peptide or the I-II linker was found to be in the nanomolar range. [23] . The modulatory role is observed when β_{1a} nulled myotubules show a decreased L-type Ca^{2+} current. [24].This is indicative of a failure in the E-C coupling process caused by a reduction in the voltage sensors. Other work in this regard by Beurg et al [25]and Sheridan et al [26] showed a more direct role of the β subunit with it involved in the actual transmission process of the signal between the α_{1S} and the RyR1.

1.2.2 β subunit and RyR1

As stated in the previous section the β subunit is very important to the normal functioning of the E-C coupling process. It was found that the deletion or substitution of these residues in particular greatly reduced the amplitude as well as the rate of depolarization-induced Ca^{2+}release by greater than 50 % [27].

.

1.3 RyR2

1.3.1Excitation-contraction coupling in RyR2

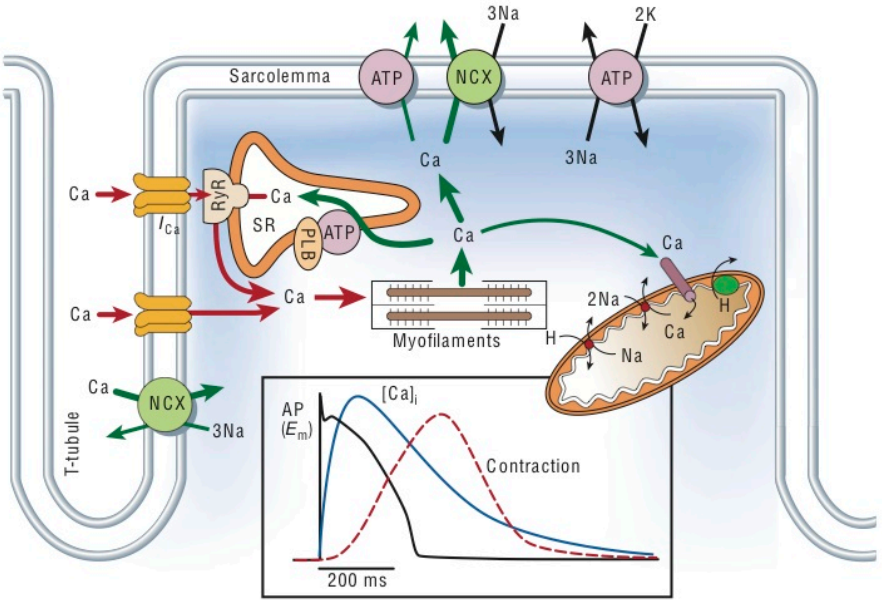

Figure 5: Excitation-contraction coupling in Cardiac Muscle

The figure above shows the time course of an action potential, Ca^{2+}transient and contraction it causes. This is measured in the case of rabbit ventricular myocytes at 37 ˚C. Abbreviations used in the figure are as follows: NCX(Na^{+}/ Ca^{2+} exchange) ATP, ATPase; (PLB) phospholamban; SR, (sarcoplasmic reticulum)[28]

The above figure is an overview of the process of E-C coupling in the case of a ventricular myocytes. It goes over the movement of the different ions as well as gives a clear graphical representation of the contraction that is achieved as a result of the entire process. This section

will serve as an introduction to this intricate process as opposed to a detailed view into each mechanism that is involved.

Excitation contraction coupling in cardiac myocytes is very different than in skeletal muscle. It however starts off in a similar fashion with an action potential. The central role in this entire process is played by the ubiquitous Ca^{2+} ion. The proper functioning of the heart greatly depends on how the cell handles calcium. Failure to handle Ca^{2+}properly leads to various pathophysiological conditions like arrhythmias and contractile dysfunction [28].

The E-C coupling process starts off with a self-generated cardiac action potential. This is the initial depolarization seen in the graphical representation of the action potential in the figure above. A calcium current (I_{Ca}) enters the cell through channels that are activated by the cell depolarization. In the case of the cardiac myocytes the Ca^{2+}channels that contribute majorly to the I_{Ca} are called L-type channels. The entry of the I_{Ca} is countered by a Ca^{2+} dependent inactivation that takes place on the cytosolic side. Hence it acts a method to limit the calcium that enters during the I_{Ca} current. [29, 30].The next step in the E-C coupling process is Calcium Induced Calcium Release (CICR) which was first described by Fabiato [31] starts when the I_{Ca} activates the RyR in this case the RyR2 isoform. The activation is then followed by an increase in the Ca^{2+}concentration in the cytosol ([Ca] i) which is also called as a calcium spark [32, 33]. Next the Ca^{2+}which was released from SR Ca^{2+}stores binds to Troponin-C this sets of a cascade of protein-protein interactions which eventually to force generation and

contraction of the myocytes. This physiological contraction involves rapid shortening of the fibers which causes ejection of blood [28].

2.1. Introduction to Cryo-electron Microscopy

Cryo-electron microscopy (cryo-EM) is a method used in electron microscopy to obtain structural details of a variety of biological systems that vary from very ordered icosahedral viruses to more complex structures like the ryanodine receptor which has very low symmetry. This introduction to cryo-EM will provide any non-microscopist a basic understanding of the how and why of cryo-EM as well as an understanding of the depth of its application in structural biology.

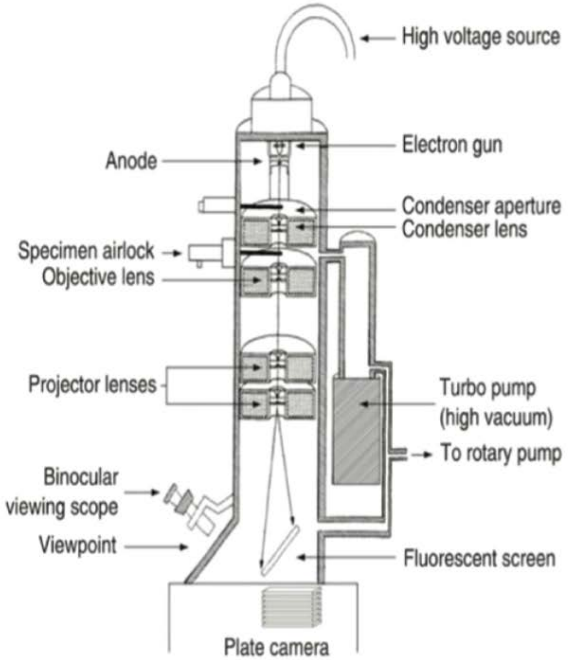

Figure 6:Parts of an Electron microscope

The overall setup of an electron microscope [34-36]

The figure above shows the various components of a cryo-EM microscope. The overall assembly consists of an electron gun, a column, a viewing chamber as well a computer to view the acquired images.

2.1.1 Lens system

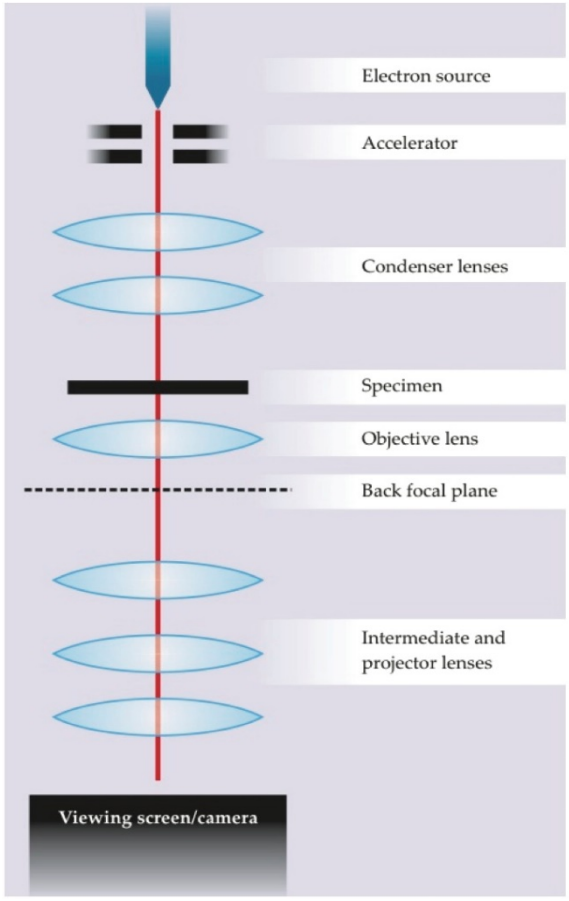

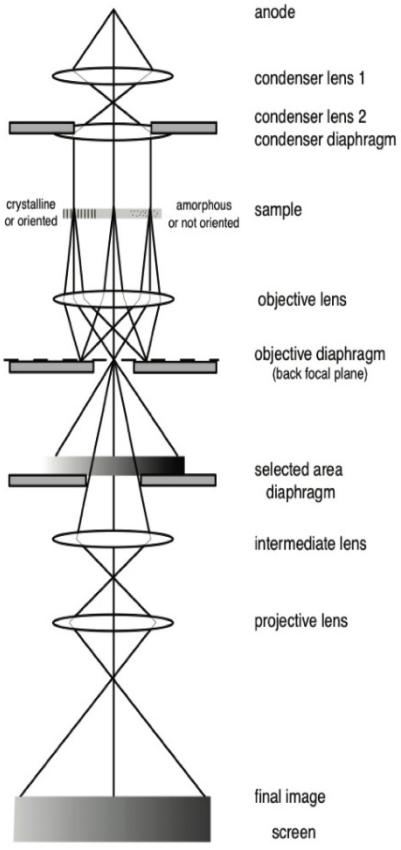

Figure 7:The Lens System

The panel on the left shows the overview of the lens system[37] inside a Transmission Electron Microscope and its associated ray diagram is on the right[37]

The figure above is a schematic of the internals of a column and shows the different types of lenses that are present. The objective lens in this system is mainly responsible for focusing and magnification of the object [38]. There are also generally two to three condenser lenses which mainly control the illumination of the sample (i.e. brightness) .The apertures control the exposure and have names that reflect and qualify their purpose in the system. The filament of the electron gun can be of various types such as the heated tungsten filament or a thermal filament made from lanthanum Hexaboride(LaB_6).These electron guns emit electrons when the work function is exceeded [34].A mention must be made of the Field Emission Gun(FEG) which does not have a thermal filament as explained in a dedicated section on FEG's in particular as they are utilized in our process. Once the electrons are emitted (in high vacuum conditions) they are accelerated down the column with the help of accelerating voltages of the order of 80-300kV. [39] Next the electrons pass through the sample and create an image. Image creation is a complex process in itself because electrons can either go through the object without any deflection, interact with the nucleus leading to a change in their direction or lastly "backscatter" following the same path as they came in. Among these different possibilities the change in direction scenario is most favorable for the microscopist because it is responsible for the generation of contrast which aids in the production of detail in the structure [38]. The generation of contrast in an electron microscope is through the interference of the elastically

scattered electrons (the electrons that backscattered) and the inelastic scattered electrons (the electrons that got deflected by the electrons around the nucleus). The objective lens brings about this interference between the two and hence is one of the most functionally important lenses in the assembly. The penultimate stage of the microscope is a series of projector lenses which function to increase the magnification before the final image is formed [37, 38] .

2.1.2 Field Emission Gun

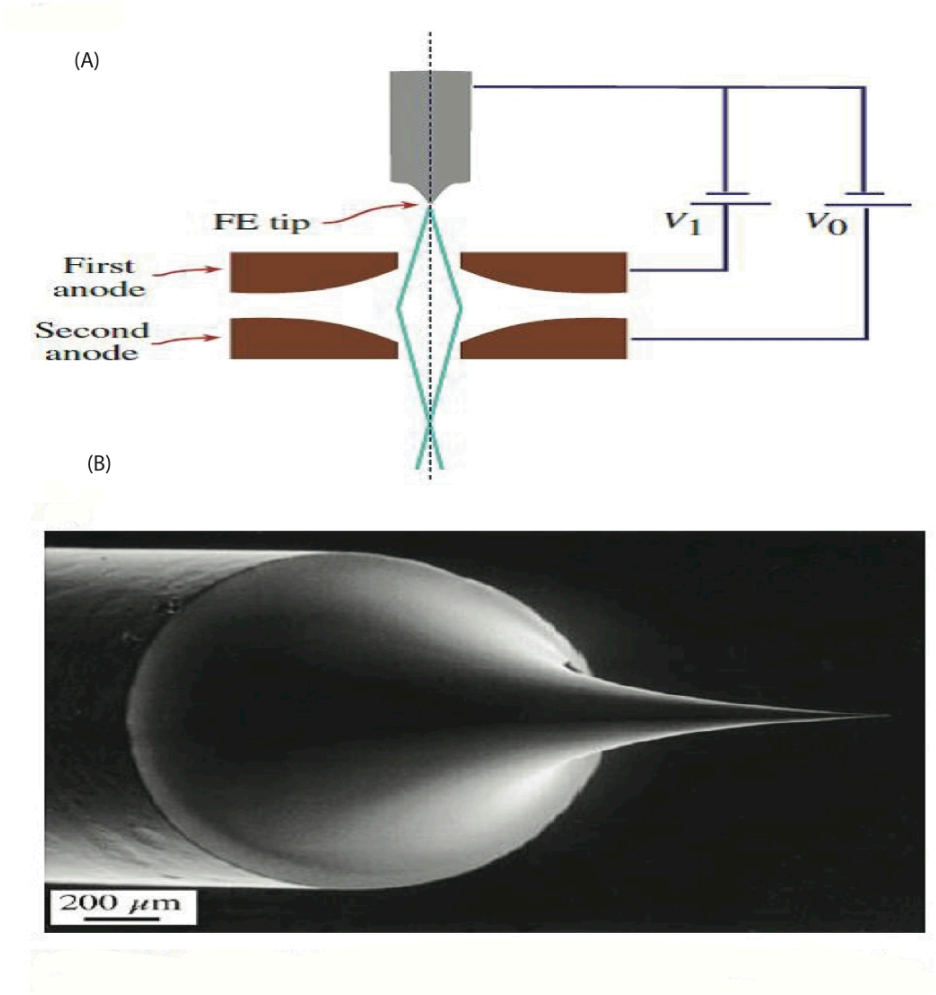

Figure 8: The Field Emission Gun

Fig (A) Electron paths from a field-emission source showing how a fine crossover is formed by two anodes acting as an electrostatic lens. Sometimes an extra (gun) lens is added below the second anode. (B) A FEG tip, showing the extraordinarily fine W needle.

The basic setup and working principle of the field emission gun is shown in the figure above. Seen in the figure is the electron gun (which acts as a cathode) and two anodes. The first anode is charged with a very high potential of several kV with respect to the FEG's tip. This high potential is also referred to as "extraction potential" [40].The process of turning on the electron gun is done very slowly by a computerized controller so as to avoid mechanical shock which may damage the tip. The second anode provides acceleration to the electrons which were extracted. The entire system is maintained under high vacuum conditions to prevent contamination of the tip. A 10^{-10} Torr vacuum will ensure a clean tip for several years. [40]. The major advantage of using an FEG is that it provides a higher β value as compared to tungsten or LaB6 filaments. It would suffice to understand that the β value gives the brightness without going into much detail of the equation that derives its value.

2.1.3 Charged Couple Devices (CCD)

The last stage is the viewing screen which can again has various types and vary with the application in question. For applications such as ours which involve imaging ryanodine receptors charged coupled devices (CCD's) are adequate. A CCD is made of a single slab of photosensitive silicon overlaid with insulating channels called channel stops. The channel stops divide the silicon slab into rows. Next the silicon surface is covered with thin coating of silicon dioxide and aluminum strips are then overlaid over as well as perpendicular to the channel stops. Thus, the overall structure that results resembles a gird. Each sectioned off portion forms a pixel and each pixel forms a Metal-Oxide Silicon (MOS) capacitor. The losses through capacitive coupling however are greatly reduced by the silicon. Each MOS capacitor by definition would store charge (electrons). Shown in the figure above is a diagrammatic representation of how the silicon surface captures an electron (in this case photoelectrons emitted by the electron gun that passed through the lens system and is finally incident on the recording CCD device) in what is termed as a potential well. This completes the exposure step.

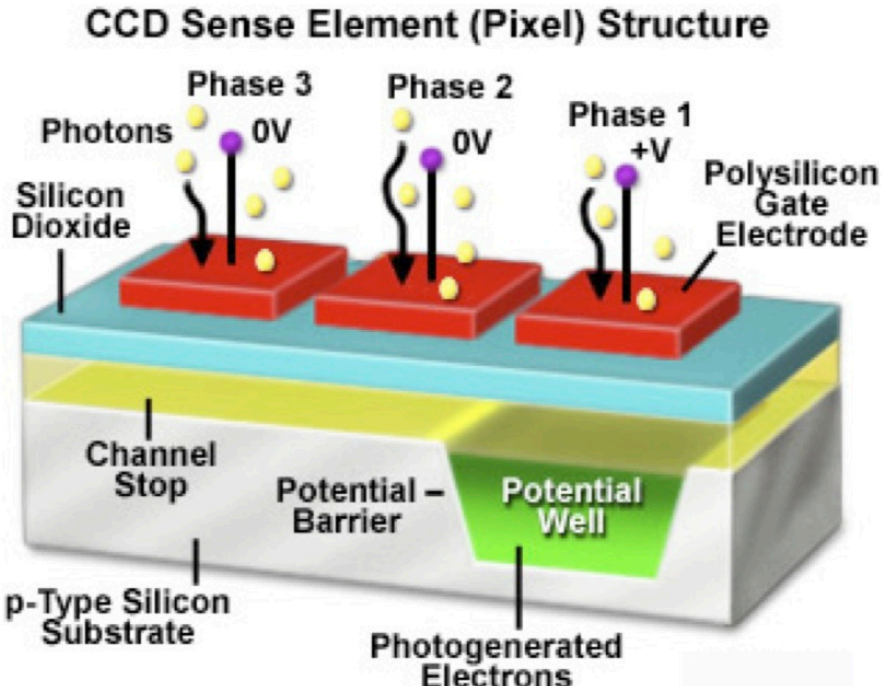

Figure 9: CCD sense elememnt

The figure is a diagrammatic representation of the CCD Sense Element in its typical 3 phase operation Charge is stored in a “potential well” and then shifted row by row to the output [1]

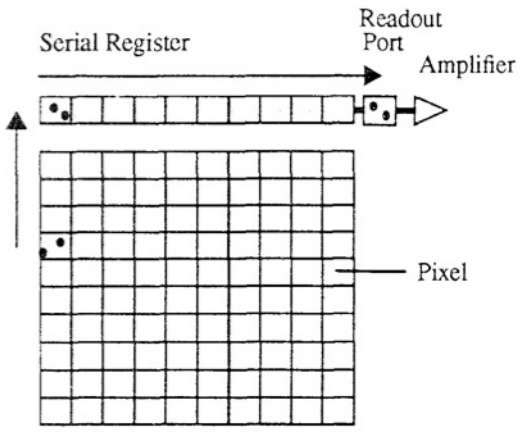

Figure 10 : Reading of a CCD

This figure shows the “Reading” step by a CCD.

After the exposure step is complete the stored charge packets in each row are shifted to a serial register and read-out with the help of a readout port. This is how the light intensity is transduced to analog voltage level. These analog signals from the different pixels can be digitalized using an analog-to-digital converter. Thus the CCD will obtain and construct an image from the various intensities that it obtains. The scientific CCD’s usually are capable of 16 bit resolution which corresponds to 65,536 gray levels thus its performance comes close to a normal light detector [41]. The performance of a CCD is measured using a parameter known as Detection Quantum Efficiency (DQE). An ideal detector would have a DQE of 1 or 100%. CCD’s are capable of having DQE’s of greater than 80%.

Using CCD’s has many advantages. Firstly CCD’s have a “Detection Quantum Efficiency” (DQE) of greater than 0.5 (the ideal DQE=1). The second important advantage of a CCD

detector is its large dynamic range which enables its use in recording diffraction patterns that have a very big span [40].

3. Sample Preparation in Cryo-EM

One of the crucial steps for obtaining high-resolution images is sample preparation. This section will look at the different steps involved in the preparation as well as the techniques used to improve image contrast. Improving contrast is a critical step in the image processing of the biological specimen.

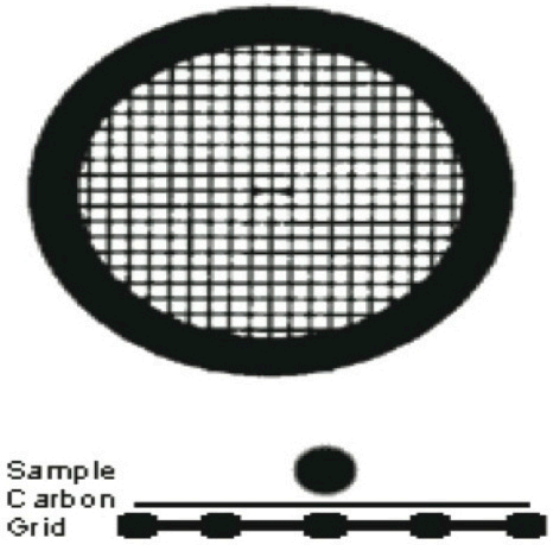

Figure 11:Basic construction of an EM Grid

The following figure shows the basic construction of an EM grid. Grids can have various pore sizes [34]

Using cryo-EM we image the macromolecule in-vivo conditions. This means that the macromolecule is in a hydrated state while it is inside the imaging instrument. To start off we will look at the preparation of an “EM grid”. An EM grid is a basically a foil mesh of a standard diameter of 3.05mm.Various metals can be used to prepare the foil mesh some examples being copper, gold, molybdenum, stainless steel, tungsten, aluminum and titanium. Although the diameter of a grid is constant at 3.05mm the thickness of the grid varies within a range of 10μm-25 μm. Grids are commercially available. The manufactured types are differentiated from each other on the basis of the number of holes per inch. In essence the EM grid is to the cryo electron microscope what the glass slide is to the optical microscope. The grid in essence acts as a support as well, as a method of delivery so that the sample can be viewed [42] .

Grids require a certain amount of preparation before they can be used. This preparatory process usually involves the coating of the grid with a carbon film. Next, depending on the application it may or may not have perforations present. The sample may either reside in the holes or adhere to the carbon itself depending on the application in question.

3.1 Holey Grids

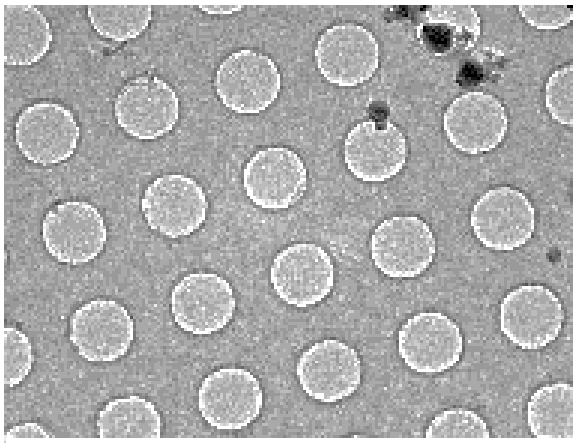

Figure 12: Holey Grids

A representation of a manufactured holey grid

Holey grids are have several advantages that make them ideal for cryo- EM techniques. One of the main functions of the holes in the grid is to eliminate any absorption and scattering by the carbon film. Cryo-EM images have a very low signal to noise ratio (SNR) therefore it is vital that any processes that lead to the development of noise be eliminated. Each hole forms a “well” or a “pocket” inside of which the sample remains completely hydrated when frozen. Keeping the sample fully hydrated while it is being imaged is what separates cryo-EM from the other TEM techniques.

3.2 Carbon Evaporation

As a part of the grid preparation carbon is that is deposited on the grid has holes in it of a specific size by the process of carbon evaporation. Here we look at the basic principle of this method but the specific parameter adjustments are mentioned in the methods section

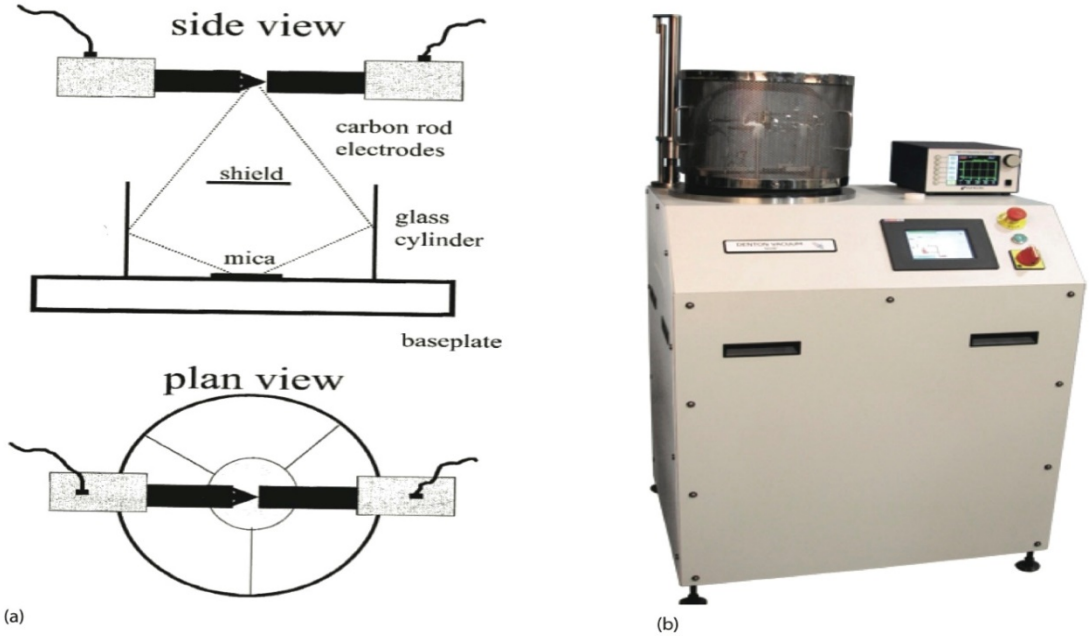

Figure 13:Carbon Evaporation

The panel (a) on the left shows a schematic diagram of the principle of carbon evaporation. Panel (b) shows the DV-502B evaporator used for this process[43, 44].

Carbon evaporation has a fairly straightforward principle. A high voltage circuit is formed with the help of graphite rods as shown in Fig: 12(a). A freshly cut piece of mica is placed in the bell jar of the carbon evaporator which is kept at high vacuum condition.

The passing of current through the rod leads to it reaching an incandescent state. When this happens carbon is actually being evaporated off the rod and deposited on the mica. Once the mica is coated it is very slowly submerged into water (preferably in a small water tank).The carbon film floats off the mica. The holey carbon side of the grid is then carefully placed in contact with the floating carbon[34, 45] .

3.3 Glow Discharge

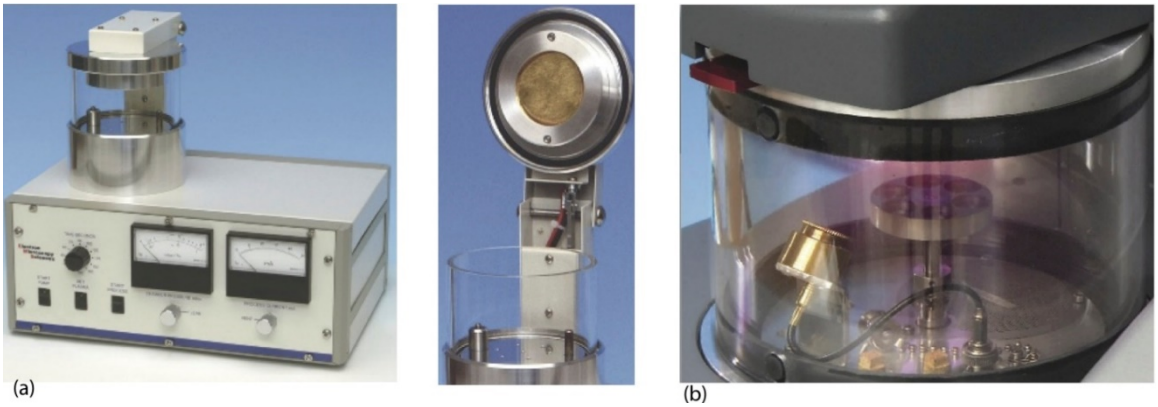

Figure 14:Glow Discharge Apparatus

Figure 14 (a) shows the E-7620 by Electron Microscopy Sciences along with a closer look at the glow discharge add-on. Figure (b) shows the “luminescent glow” that is normally observed in a glow discharge chamber [46].

Figure 14 (a) shows the E-7620 by Electron Microscopy Sciences along with a closer look at the glow discharge add-on. Figure (b) shows the “luminescent glow” that is normally observed in a glow discharge chamber [46].

The glow discharge step is performed in reduced atmosphere and is a well-known and accepted method to make the surface of carbon hydrophilic. A standard glow discharge device is shown above. The process involves placing the grid between two electrodes in an evaporator at high voltage [47].

3.4 Sample Vitrification

Figure 15:Sample Vitrification by Vitrobot'[48]

One of the vital steps in the process of sample preparation specifically pertaining to the cryo-EM technique is vitrification. If water present in the biological sample is cooled slowly it leads to the formation of crystals. The crystals that form damage the macromolecule and distort its structure. From the point of view of a structural biologist it is essential that the structure

remains intact. Through vitrification the sample is cooled at a very fast rate avoiding crystal formation completely and thereby preserving the structure [49].The “Vitrobot Mark IV” is used for freeze plunging the sample. It has a lot of advantages compared to conventional methods. The greatest advantage other than the obvious one of automating vitrification is high throughput and reproducibility. These advantages can be attributed to the highly controlled environment that the vitrobot provides.

The figure above shows the “Vitrobot Mark IV” by “FEI”. It consists of several parts such as a sample holder (which can be filled with Liquid N_2, blotting pads to remove the excess sample, and tweezes to hold the grid with the sample in place during the plunging process. The Figures below show enlarged views of each component for the sake of clarity

Figure 16:Up-close with the Vitrobot

Fig 16 (a) shows the overall holder which also holds the liquid N_2 (b) Shows the assembly that holds the tweezers with the grid, it also shows the sample being loaded onto the grid before it is plunged into the bath. (c) Shows a close view of the bath with a sample store after it has been plunged (d) shows how the tweezers are attached to hold the grid before the sample is loaded.

The specifics of the plunging technique will be revisited in the methods but the overall goal of this technique is to use the Vitrobot to cool the sample and grid system at a very quick rate so as to vitrify it and preserve the sample in its native state. The vitrobot also has a very

controlled atmosphere in which interaction with any contaminants can be prevented and environmental parameters like humidity can be controlled

4. Image Processing of Cryo-EM Samples

When considering the image processing steps for the cryo-EM samples there is a lot of considerations that one must take into account. The design of the processing workflow varies depending on what is being imaged and the features that the macro-molecule contains .This section will outline the overall methodology for imaging of the ryanodine receptor in particular along with some basic concepts of imaging and three dimensional geometry which form the basis of these techniques.

4.1 Introduction to Euler's angles

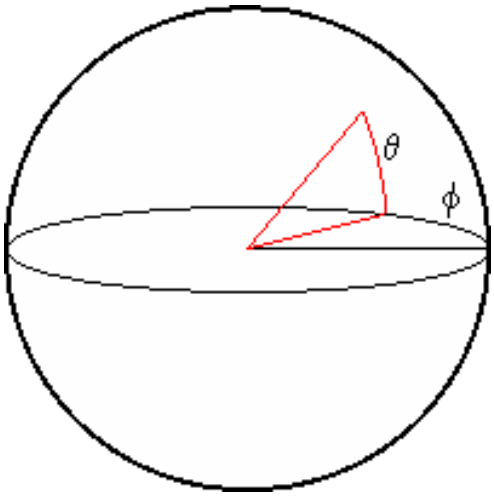

Figure 17:Euler angles

Figure showing the three Euler angles theta (θ), psi (ψ) and phi (ϕ) which are obtained by rotations about the different axes [34].

The position of a three dimensional object is defined by the Euler angles theta (θ), psi (ψ) and phi (ϕ). The figure assigns θ as the elevation, ϕ as the azimuth or rotation around the vertical axis and ψ as the is the rotation about the center which is defined using θ and ϕ [34]. The sphere on the whole is called the Euler sphere and the center of this sphere is where the sample is. The definition of which angle corresponds to rotation about which axis depends on how it is defined by the reference

4.2. Overview of the Image processing workflow

In this section we look at the overall image processing workflow and how one goes from having from having two dimensional images of the RyR to a three dimensional RyR. Cryo-electron microscopy gives images at very low contrast. In order to obtain high resolution structures we require to utilize a number of software packages which help in gathering the best out of our dataset.

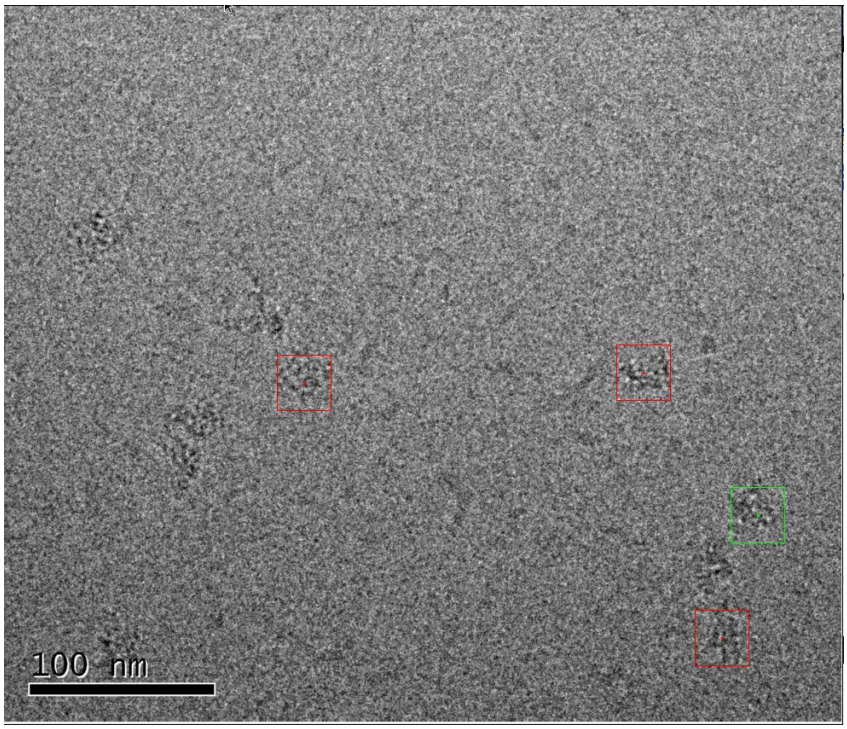

Figure 18: Particle Picking

Particle Picking using EMAN2 Boxer

4.2.1 Picking Particles

The image above shows the particle picking program “boxer” which is a part of the EMAN2 [50] suite. The boxed particles can be saved in SPIDER [51] format. It contains information about each box containing the particle. This selection procedure is continued for each image. A reference three dimensional model is required at this step. This reference volume has its corresponding parameter file containing every possible orientation of the ryanodine receptor. We used the RyR1 as our reference model because it shares a very high sequence homology with RyR2 [52-54].Projections of the reference are made from every orientation and the

angular information is stored in the corresponding “parameter” file of the reference. The parameter file is a tab delimited file containing the particle number, the three euler angles (ψ,θ,ϕ),shit in the X-direction(X SHIFT),shift in the Y-direction(Y SHIFT),magnification, defocus, astigmatism and arc cosine of the correlation coefficient (which signifies the correlation between a particle in the experimental stack and the reference model)[55].The next step would be to create an image stack containing the boxed particles. This image stack contains boxed particles. Comparison of the image stack with the reference image stack is done using FREALIGN.[55]. In a very overly simplistic way FREALIGN compares each image in our experimental stack with the reference model to find how similar it is to projection in the reference. An overview of the various inputs and outputs is shown below.

4.2.2 FREALIGN-Fourier Reconstruction and Alignment

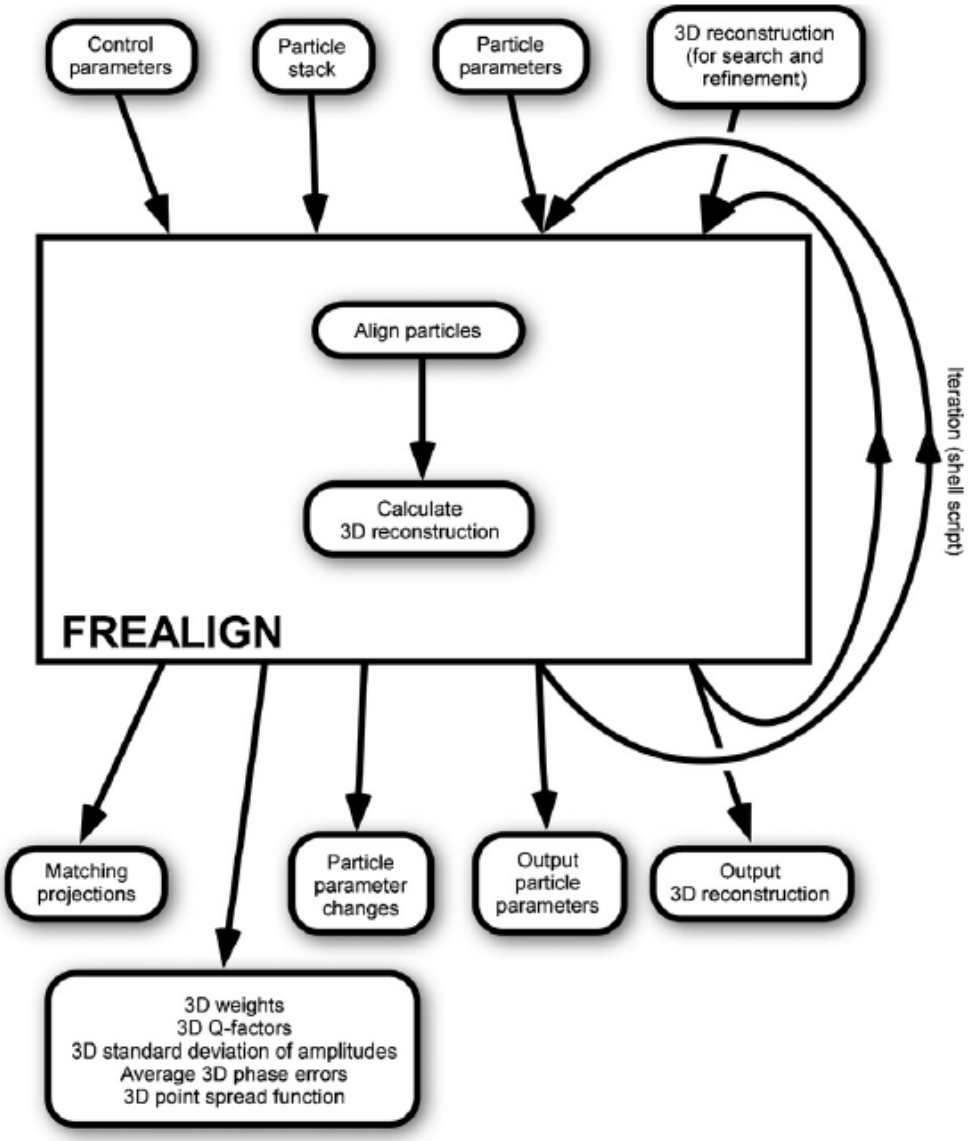

Figure 19:FREALIGN Parameters

A flow chart showing the working of FREALIGN [55]

The figure shows the iterative procedure that FREALIGN uses during the process of refinement and reconstruction. The iterative nature of this algorithm ensures that the particle parameters are updated and hopefully, improved at every step. The new particle parameters will then serve as the input for the next loop. FREALIGN also does what is known as CTF correction along with reconstruction and refinement of the reconstruction. Contrast Transfer Function or CTF is a measure of how the cryo-electron microscope is “seeing “the electrons and forming the image.

5. Structure of Ryanodine Receptor

The final step after the steps of picking and processing using FREALGN is viewing the final structure of the RyR using a software package called Chimera [56]. Using the three dimensional volumes that are obtained the structure is further processed in a directed manner so as to obtain a final structure with the highest possible resolution. Certain features of the RyR which are prominent are its 4 –fold symmetry. All the isoforms of RyR i.e. RyR1, RyR2 and RyR3 have a cytoplasmic assembly. The assembly that accounts for more than 80 % of the receptors mass has 10 loosely packed domains along with a transmembrane domain. [57]. The structures that were reconstructed were exposed to conditions that either promote states where the channel is “open” or “closed”.

The structure of the RyR was initially reported in the early 1990’s by Radermacher et al at the Wadsworth Center in New York [58] and also by Serysheva et al in the Baylor College of Medicine [59] . The figure below by Samso et al [57] shows a larger structure (which is marked in fluorescent green) and a smaller structure (marked in fluorescent pink). The structure demarcated by the fluorescent green is highly convoluted and bears resemblance to a 280 x 280 x 120 Å square prism in terms of shape. This is the cytoplasmic region of the receptor. The smaller region which is marked in pink represents the transmembrane region of the receptor [58].

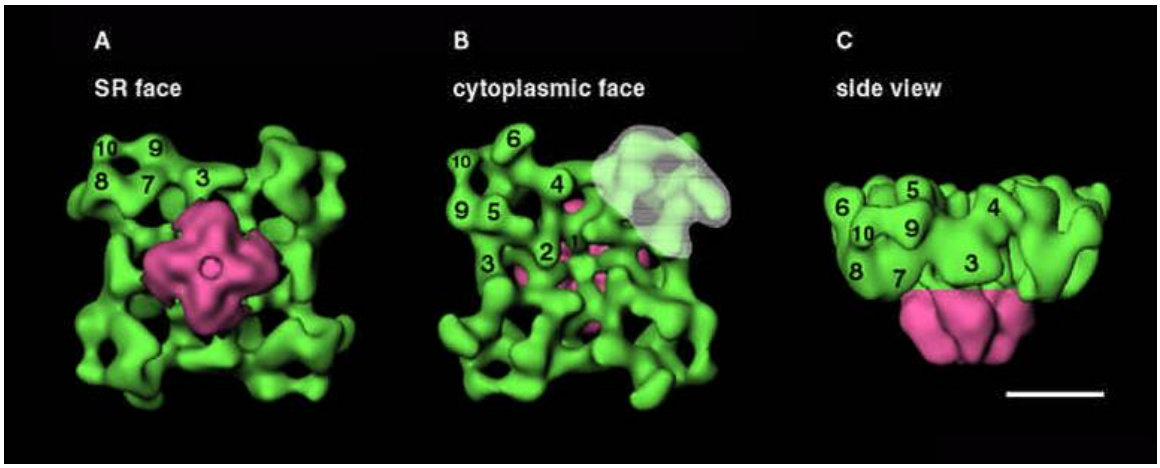

Figure 20:Ryanodine Receptor Orientations

The figure shows the 3 different orientations of the RyR. Figure (A) is the view of the RyR onto the SR face. The orientation shown in (B) is the exact opposite of the one shown in (A). The white area highlights one of the four regions in the RyR that has a very high probability of reacting with a DHPR. [57]

5.1Cytoplasmic Assembly region

The overall structure of the cytoplasmic domain consists of 10 globular domains per subunit. Radermarcher et al [58] numbered these domains in a completely arbitrary manner. The Baylor group [59] named the four large “3” domains , which are also the largest domains as “handles”. The domains 5-10, which form the corners of the cytoplasmic assembly were given the special name of “clamps” by the Baylor group. Domains marked as “2” surround a solvent filled pocket and have a diameter of 40-50 Å.

5.2 The Transmembrane assembly

The transmembrane assembly is marked in pink in figure 20. According to the view in panel A of the figure, when the receptor is viewed along the 4 –fold symmetry axis and onto the face containing it (as seen in Fig 20(A) the transmembrane domain appears to have the overall shape of a square. Compared to the cytoplasmic assembly the transmembrane domain appears to be rotated by 40 degrees. The side view shown in panel C shows that the transmembrane domain appears tapered. This is in comparison to the end that is connected to the cytoplasmic region which has a larger diameter of 120 Å. The TM domain has a length of about 70 Å. The shape of this transmembrane domain varies between different reconstructions (which are determined independent of one and other). This variation is likely to be due to the presence of a variation in the functional states of the receptor [57] but there are several other factors which may also contribute. Closer observation of the different reconstructions led to the observation of a 20-30Å column of low density .This low density column was indicative of solvent accessibility. This low density column lies along the 4 – fold symmetry axis of the transmembrane domain as shown by Radermacher et al [58]. The receptor exhibited very interesting behavior on treatment with ryanodine. Functional analysis showed that the ryanodine locked the receptor in an open or partially open state. Furthermore, it was observed that the that the column of low density became better defined appearing to form a channel across the region [60]. This channel that is formed is believed to be the wider regions of the ion conducting pathway. This argument is heavily supported by the virtue of it being analogous

to the known structure of the potassium channel from Streptomyces lividans [61] . Being a tetramer too this channel is believed to be structurally homologous to the RyR especially in the region of the transmembrane pore [62-64]. . There are few questions that the single pore model does not account for. The first question is with regard to the discrete as well as evenly spaced sub-conductance sates that have been reported. [65, 66] . The single pore model does not account for this. There is the possibility that there exists four independent pores that are "allosterically coupled" to each other .Allosteric coupling as per Sayar et al [67] is defined as the "propagation of a perturbation (such as the binding of a ligand) from one part of a protein molecule to another part".

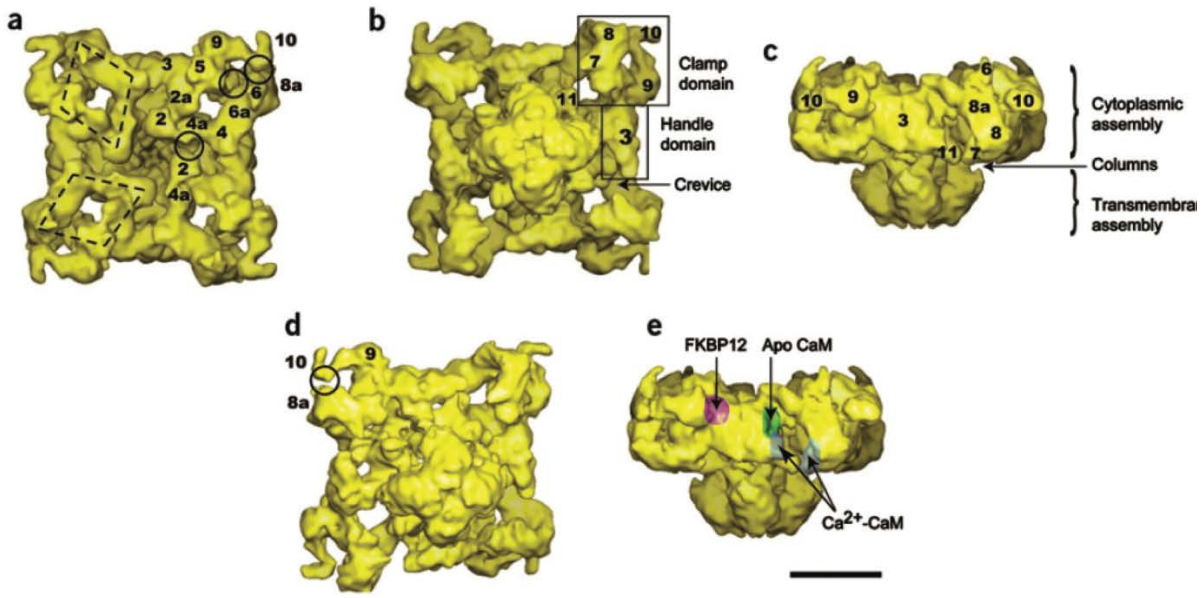

Figure 21:Isosurface Representation of RyR1

The various views of RyR1 labelled from (a-e) showing the T-tubule view in (a) SR view is seen in (b, d) and side-view seen in (c, e). Scale bar 10nm

In the figure above the clamp domains (7-10) can be seen with greater clarity. These domains now appear to be formed from two separate structures. The first structure appears to be located at the outer corners of the square prism (8a-8-7). The second structure appears to be an "elongated and tapering structure that extends by the side of the square and towards its corner (domains 9-10) [68] . The figure 21 (d) shows a self-standing element that makes a protrusion towards domain 8a. There is also a distinctive kink that is seen in domain 10 which is seen in both Figure 21 (b) and (d).

Tubular structures are seen in the region that faces the t-tubules. The most distinctive feature however is the geometrically rhomboidal structure that is defined by the domains 2-4-5-6. This rhomboid structure is seen in other RyR1 structures also. Samso et al [68] suggest that the inter-relation between the various domains mostly occurs in regions where certain bulks of mass come in close proximity to each other . Speaking more specifically there are three such regions per subunit. The domains that are involved are (2-4a') (4a' is the 4a domain from an adjacent rhomboid structure), 5-6 and 10-8a (these areas are indicated using the circles in the Figure.1. Domain 3 is an example of a handle domain that we have mentioned on the previous section. Also, seen in the figure in panel (c) is a crevice bounded by domains 3, 4,8a and 8 respectively. This was described as a tilted canyon that extends from the SR side to the T-tubule side. There is also a new domain in the reconstruction that is which is shown in panels (b) and (c) labelled as 11. It is essentially a protuberance from the cytoplasmic assembly on the proximal part of the SR side.

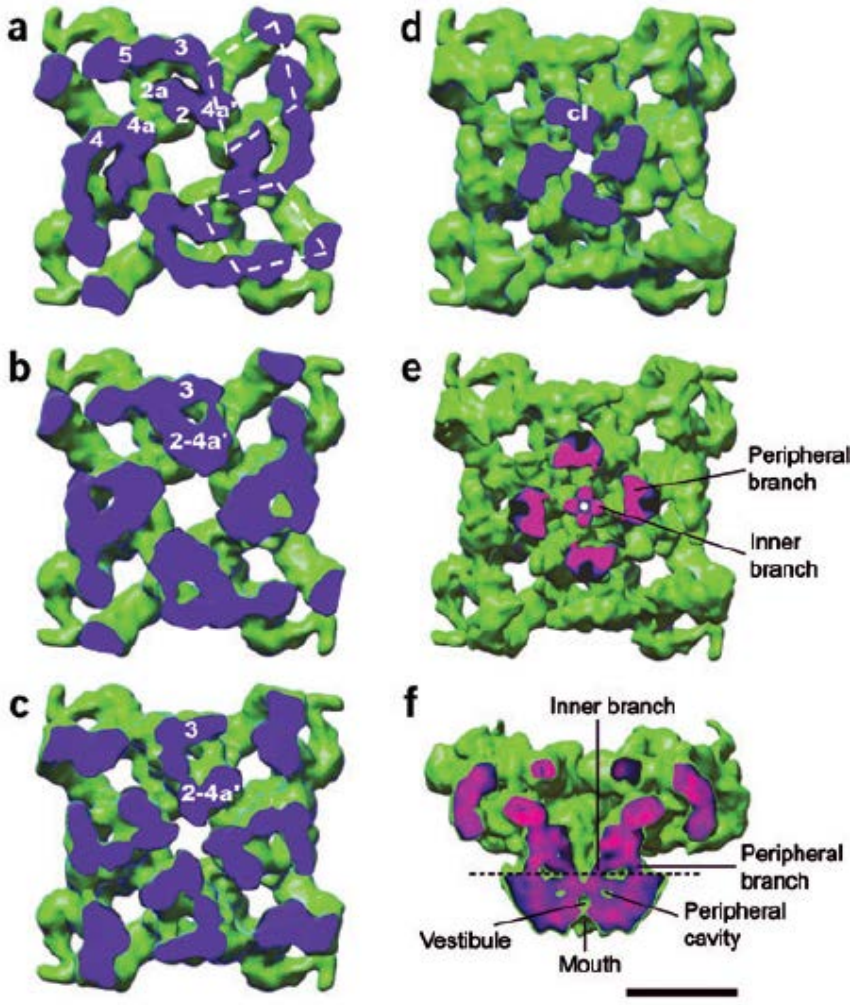

Figure 22: Structural Assembly and Columns

The figures in panel's a-f intend to show the various mass alignments as well as the inter-domain interactions. The multiple figures in the panels above show successive sections of the cytoplasmic assembly .The blue in the figures on the left hand side represents the sectioning plane. Panel (a) shows the interconnection between the cytoplasmic domains. Below the T-tubule facing surface domains 2 and 4a' occurs the fusion of the rhomboids (shown by the

white dashed lines). The domains 2a and 3 have an interconnection through a secondary bridge of density and connect with 2-4a'.Therfore a column of density is formed by the fusion of domains 2-2a-3-4a'. The 4 columns can clearly be seen in panel (d), one of the columns is labelled c1. It is the merger of these 4 columns that eventually leads to the formation of the transmembrane domain. The formation of the transmembrane assembly is clearly shown in panel (e).The panel (f) is a side view showing the 2 branches of each column. The color coding convention used is pink for the denser areas and blue for the less dense structures. [68]

Increasing resolution is the primary aim of three dimensional reconstructions. The improved resolution achieved by Samso et al [68] has allowed for the identification of a region of separation between the transmembrane and cytoplasm domain. Seen in panel (c) are 4 columns that measure 14Å in height that span this gap. They are given the name of "columns" for ease of identification. They are formed from the SR proximal part of the cytoplasmic assembly that is shown in the figure. A non-uniform distribution in density was observed with the peripheral branches and internal branches having a considerably higher density.

5.3 Detailed look at the transmembrane structure

In order to completely understand and appreciate the effect of the introduction of the Mg^{2+} ion to the skeletal isoform of RyR it is imperative that we have a clear understanding of the mechanics that are involved in the opening and closing of the ion pore and their subsequent implications so that a wholesome, well rounded understanding of the pore gating is formed.

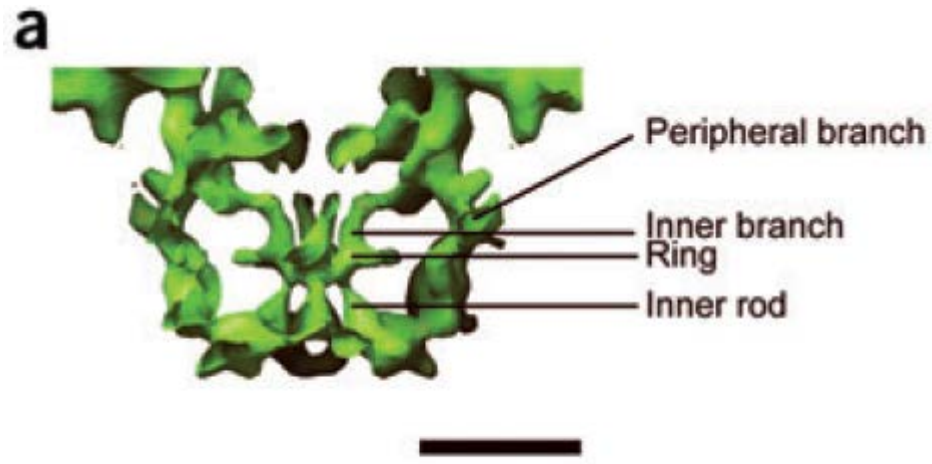

Figure 23: Substructure of the transmembrane assembly

The figure shows the transmembrane sub-structure consisting of peripheral branches, inner branch ring and the inner rod. Scale Bar 5nm

The figure above is a central slice of a side view of the transmembrane domain. The structure is viewed at a very high threshold so as to display the rod structural details. Overall four rod structures of high density are observed connected to the ring structure which also has high density. The merging of the four columns leads to the formation of definite external

boundaries of the transmembrane square prism structure. This is seen in the panel above as well is in (e) of figure 22.

6. Methods to measure the quality of a reconstruction

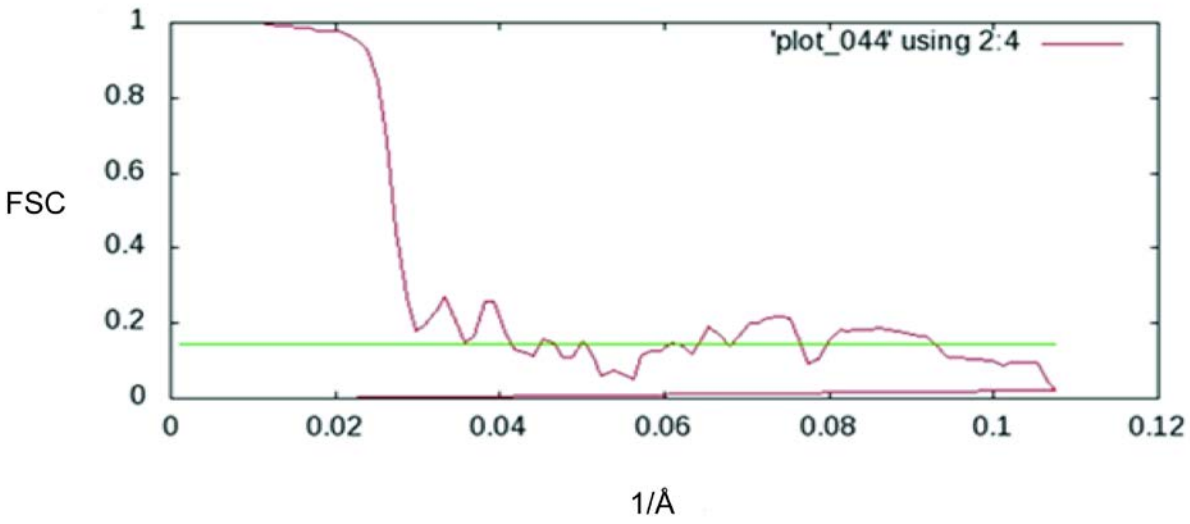

Figure 24:Fourier Shell Correlation Curve

This is an example of an FSC Curve with FSC values plotted on the Y axis and the inverse of resolution in angstroms (1/À).The green line demarcates the FSC value of 0.143.

The figure above is an example of a “Fourier Shell Correlation” curve. It is defined as the “modulus of spatial frequency whose values are correlation coefficients calculated between the Fourier transforms of two images/volumes over rings /shells of approximately equal spatial frequency”[69]. FREALIGN constructs two volumes for a single reconstruction run. From

even and odd particles. The FSC curve gives the correlation between these two so called half data sets. FSC values which are plotted on the Y-axis range from 0 to 1. This essentially means that at FSC =1.0 there is complete correlation between the two three dimensional volumes. Negative FSC values also exist which imply inverted contrast. The X axis of the graph is the inverse of the resolution in angstroms. The curve shown in the figure shows the 44th iteration of the RyR2 dataset in the open state as an example. The solid green line shown corresponds to an FSC value of 0.143.The FSC value of 0.143 is used if and only if secondary structure is visible.

7. Effect of Mg^{2+} on the Ryanodine Receptor

Magnesium is a known inhibitor of the ryanodine receptor.[70-72]. Since it is present a physiological system, understanding the effect that Mg^{2+} has on the RyR1 is vital. Along with Mg^{2+}, ATP is also present. The activating effect that ATP has on the RyR1 has been established by several studies [73, 74]. Though it is possible to activate the RyR1 without Ca^{2+}, the presence of Ca^{2+} ensures maximum activation.[73, 75, 76].

Through the work of Samso et al [77] the 3D reconstruction of the RyR1 in the open and closed state has been elucidated. The 3D maps that were obtained had a resolution of 10.2 Å at an FSC (0.143). This systematic study compared 2 datasets one locked in the open and the other locked in the closed state.

They used the RyR1 with FKBP12 (which is an FK506 binding protein and is known to bind to RyR1 [78, 79]. When it binds to the RyR1 it stabilizes the channel either in the open or closed state. Most importantly it eliminates sub-conductance states [78].

Samso et al used RyR1-FKBP12 channels with neuroactive noncoplanar polychlorinated biphenyl 2, 2′, 3, 5′, 6-pentachlorobiphenyl (PCB 95) since it had an activating effect on RyR1 [80, 81] having the overall effect of keeping the channel open. The mean open probability (Po) that they recorded was 0.96.

In order to simulate the closed state 2 mM EGTA was used had the effect of closing the channel completely (Po=0). Using [^{3}H] ryanodine binding experiments (which query the conformational state of the RyR [82]) they showed that the specific binding of [^{3}H] was negated completely. This conclusively showed that RyR1 was in a completely closed state in the presence of EGTA. Conversely the presence of PCB95 produced 10 pmol of binding sites per milligram of SR protein. This conclusively showed that the RyR1 was completely open under these buffer conditions.

These 3D reconstructions open and closed states were significant advances in understanding the mechanism of gating in the RyR1. Comparison of the RyR1 in the presence of Mg^{2+} and ATP to the maps by Samso et al helps put the reconstruction obtained into perspective. For the complete comparison of these reconstructions as well as their implications refer to the results and discussion section.

8. Noise Bias in Cryo-EM

Imaging of the biological specimens through cryo-EM has advantages like being able to able to image the system in low dose conditions. However this advantage comes at the cost of contrast. The negative staining process for example, uses a heavy dye like uranyl acetate to stain the cells. It should also be mentioned that the structure being observed is dehydrated and hence is different structurally as when viewed in-vivo. We get a much higher contrast using the negative staining method as compared to cryo-EM. The low dose, non-stained conditions in cryo-EM mean that the images that result are very noisy. Exposing the samples to higher doses of electrons causes radiation damage to the sample. Therefore overall, in the image there is the view of the RyR which is termed as signal, since it is the intelligible part of the image as well as high frequency, random noise. The high resolution, high detail features of the RyR receptor which are important correspond to high frequency components of the image when converted to Fourier space. Since both noise and the high detail structures correspond to high frequency in Fourier space noise tends to be interpreted as signal and vice versa.

Though this section will focus on the problem of noise bias. However, the importance of sample preparation and image acquisition must not be undermined. Practically speaking the quality of a dataset heavily depends and is limited by the quality of the images acquired. The quality of images in turn depends on how the sample was prepared.

In this chapter we will take a look at two datasets namely the RyR1isoform with Mg^{2+} and CHAPS in a physiologically closed state and the RyR2 isoform in the presence of Amphipol.

Henderson et al [83] while speaking about the various pitfalls that the field of cryo-EM faces today cautions about the ability of those involved to differentiate between theoretical potential of a particular dataset and what can be practically achieved. He also reiterates the importance of using scientifically sound validation methods in order to distinguish true structures from complete artifacts. Since the process of refinement and reconstruction is iterative the reference structure is constantly adapting to what the algorithm believes is the best representation of the structure using the provided image stack. To exemplify how random noise can be aligned into intelligible features with an appropriate reference he shows how an image of Einstein can be obtained completely from random noise. The figure below shows the image of Einstein from noise [83, 84]

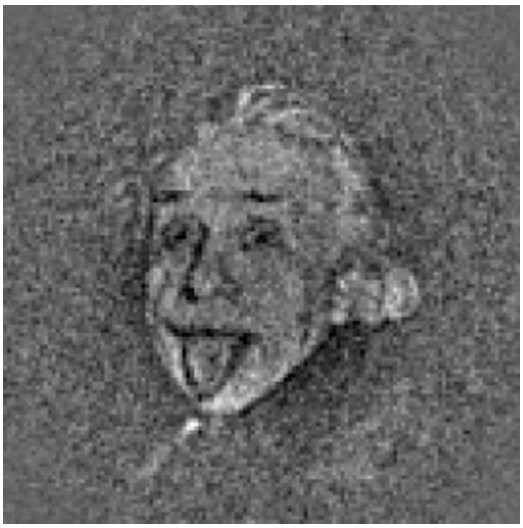

Figure 25 Einstein from noise

:

To tackle the problem of noise bias Henderson suggests several steps in order to validate the reconstruction of a particular biological sample. One method would be by using gold standard Fourier Shell Correlation (FSC) curves .According to this method the initial single particles are divided into two completely independent groups at the beginning of the analysis. Complete independence of the two groups prevents the introduction of any false correlation in the processing methodology [85, 86]. This also prevents High Resolution (HR) noise from becoming a part of the structure caused also known as HR Noise substitution [87].We will look at how the problem of noise bias affected us in the results and discussion.

9. Materials and Methods

9.1 Cleaning

We will now look at the method used to prepare holey grids. The grids that were used were Quantifoil Cu 400 Mesh holey grids (Q-10525).Since we used commercial grids we recommend that they be cleaned before use so that any residual polymer is removed. To do this we placed a layer of small contiguous glass test tubes with a filter paper layer on top of them in a petri-dish. After the cleaning process was complete the grids were placed on a filter paper with the holey carbon side facing upwards. Next the paper was wet with several drops of chloroform using a glass Pasteur pipette until they just began to float. For the final step of this stage the petri dish was covered leaving the lid slightly open in a fume hood overnight [45].

9.2 Carbon Evaporation

The second stage of the preparation process involved carbon evaporation. Mica pieces were cut using tweezers. The two new surfaces that are created were exposed by placing them face-up on a piece of paper in a petri dish. The petri dish was then placed in the bell jar of the carbon evaporator and pumped down until a vacuum of below $2x10^{-6}$ Torr.
Pre-evaporation was performed to remove any impurities on the rod with the petri dish fully covered. After this step is complete the bell jar was aired with the petri-dish cover removed. Next, a pump down sequence was performed till the vacuum reached 10^{-6} Torr. The mica was then coated with a very thin layer of carbon of the order of 5 mm .The thickness of the

carbon layer was monitored by the resulting darkness of the paper that was placed below the mica sheets [45].

9.3 Transfer to Carbon Support

In this step a 0.5 x 1 cm piece of the coated mica was cut. Carbon was then floated off onto the flat surface of filtered deionized water the flatness of which was obtained by using optical paper. With the help of tweezers the holey carbon was then placed in contact with the floating carbon layer and subsequently picked up. The steps were repeated till sufficient number of grids were prepared [45].

9.4 Glow Discharging the Grid

To perform the glow discharge the grids were placed with the carbon side facing up in a 7.5x2.5 glass slide which was covered with parafilm. The grid was then placed into the chamber and the bell jar was pumped for 20s at 25mA and 7 x 10-2 mbars. A light purple glow was observed .It must be noted that the glow discharged grids must be used within one hour of completing the discharge process otherwise they need to undergo the glow discharge process again [45].

9.5 Plunge Freezing

As a general precaution it is advisable to wear proper footwear and gloves during the course of this procedure to protect yourself from splashes from nitrogen and ethane it is also recommended that only 8 grids be used per session so as to prevent contamination. The plunging apparatus used here was the “Vitrobot Mark IV” by “FEI. The Vitrobot was switched on and allowed to complete the booting process. Next, the humidifier reservoir was filled.

Using the touch interface, the plunging conditions such as blot time, blot force and absorption time were set. The temperature for our experimentation was set at 22^{o}C. Relative humidity was set to 95%. Blot time, blot force and absorption time were set to 2s, 2 and 40s respectively. The inner holder with the ethane was cooled with liquid nitrogen until stability was reached (The process took 10 minutes to complete). Ethane was introduced into the inner chamber. The ethane which was stored in a pressurized container (Airgas 371745) had a 99.99 % purity percentage. It underwent two phase changes, one from pressurized liquid to gas as it is comes from the tank and the other from gas to liquid. The liquefaction of the ethane in the inner chamber was a result of the chamber being cooled by liquid nitrogen. After the ethane was introduced into the inner chamber it was time to load the grid onto the tweezers. This loading step involves the loading of 3-5µL of sample onto the dull side of the grid. We then waited for the sample to be absorbed by the grid before performing the blotting. Blotting is important because it removes excess sample and the helps in the creation of a thin layer. The proper alignment of the tweezers was checked before the immersion step. Once the alignment was precise immerse the grid was immersed into liquid ethane. The tweezers-grid assembly was steadily removed and transferred to the grid holder. Care was taken to ensure that the entire assembly is submerged into the liquid nitrogen.

9.6 Transfer the Grid to the Cryo-TEM

The cryo-holder was inserted carefully into the workstation without damaging the tip. The "O loop" was checked for dust or particulates using a loupe. The dewar of the cryo-holder and the workstation vessel was then filled with liquid N_2.The cryo holder was connected to the cold stage controller to help monitor the temperature

Liquid nitrogen was added till the temperature reached -194 ^{o}C. The grid tweezers, clip ring, a set of large tweezers and a screw driver were precooled using liquid nitrogen. This was followed by the transfer of the cryo grid box that contained the frozen hydrated samples.

The clip ring was placed on top of the grid and gently pressed in order to secure it. Lastly the cryo-shutter was closed so that the sample is secure and protected.

9.7 Image Acquisition

The sample was then placed on the grid the images of the sample were acquired by imaging the area next to but not directly on the area that was intended to be imaged. This process is called defocusing and reduces the radiation damage to the actual intended region. Defocusing also increases contrast.

9.8 Image Processing Workflow

After all the images were acquired they were made into an image stack. The stack contains all the images acquired and care was taken to include multiple views of a specimen in order to ensure that there was no bias introduced due to the predominance of one particular view of the specimen. The parameter file was made with the help of scripts and as mentioned in the introduction contains the Euler angles (psi, theta and phi) as well as the X and Y shifts with respect to the reference. We continued the process by providing FREALIGN software [55] [FREALIGN Version 8.04 Janelia Farm, Virginia] with a 3D reference (we provided the RyR1 3D structure), a parameter file that contained the three dimensional angular information and the stack containing the boxed particles. We started off in Mode 4 which will hereby be referred to as “search” mode. In this mode each particle finds its position with respect to a reference. There are several scripts written in various shells (BASH, CSH etc.) that were used in order to submit a job to VCU’s Teal Cluster. The cluster is a collection of parallel computing nodes which considerably reduces the time taken to complete a single iteration under the computationally expensive mode 4. Depending on the parameters of the search and the stage at where the reconstruction is a single iteration takes between 24-48 hours to complete. A script was used to calculate the percentage of particles that were moving significantly during an iteration. The reconstruction loops were continued till a stable structure is achieved. Stability usually occurs when the percentage of shifting particles is reduced to anywhere between 2-5 %.

A successful search results in a structure where each particle has found its appropriate position with respect to the reference structure. After the search is completed we changed the mode of FREALIGN to mode 1. Mode 1 or “refinement” basically does a local, less intensive search improving on the results obtained from search mode 4. Once mode 1 is complete the projections and shifts were written out and served as input for the next iteration.

Microscope parameters such as accelerating voltage, spherical aberration of the lens (Cs) etc. were provided to FREALIGN (along with other FREALIGN parameters) using a simple text file. Though microscope parameters are fixed for a given microscope and lens system some parameters like PBC and thresh_reconstruct can be optimized in order to get the most information from a given dataset. PBC is a resolution dependent weighting parameter. A high value like 100 will give equal weight to each particles. The other parameter, thresh_reconstruct is a number between 0 and 1. It controls the percentage of particles that are too be included in a reconstruction. Trials were prepared and decided based on individual ranges of each parameter. The best structure with its set of optimized parameters was used the further processing steps. We will look at the effect of these parameters in the results and discussion section on the effects of noise bias.

Finally, the results of each iteration were visualized in Chimera [56] [V1.9 San Francisco CA] . Chimera allows us to visualize the resulting three dimensional reconstruction. Various distances of the resulting structure were measured in order to validate our final reconstruction.

Chimera allows the user to cut the resulting 3D structure along different planes. We did this in order to visualize density in the transmembrane domain. This was done with a side view of the structure.

Several other views and sections of the RyR1 were obtained for more details see the Results and discussion section. Fourier Shell Correlation (FSC) curves were plotted from the resolution files of each iteration in order to monitor the resolution. They were plotted using GNU plot which is an open source software for plotting graphs and is usually included in UNIX, UNIX-like as well as Linux distributions. The FSC values at FSC (0.5) and FSC (0.143) were monitored along with the values of phase residual and the average shifts in order to observe any noticeable trends. Plotting of FSC curves is a necessary step in order to measure the final resolution of the structure.

Manual intervention is sometimes needed if the reconstruction gets stuck at a local maximum and the resolution does not reduce further. This intervention includes manually filtering out the bad views which are observed using SPIDER WEB[51]. Classes are sets of images containing a particular view of the RyR. Removal of bad classes hence is a way of giving the algorithm human intelligence, which in complex image processing is sometimes necessary.

10. Results & Discussion

This section will contain the results of my image processing work as a part of the laboratory group. I credit Dr. Vanessa Cabra, Dr. Pablo Castro as well as Dr. Montserrat Samso for sample preparation. Dr. Castro collected the images used for the reconstruction of the RyR1 with Mg^{2+}. The collection of images for the RyR2 dataset was done by Dr. Cabra.

The images of both the RyR1 with Mg^{2+} in the presence of CHAPS dataset as well as the RyR2 with Amphipol dataset were obtained using the F-20 Tecnai microscope by FEI. The microscope used for the RyR2 data situated in the department of Physiology and Biophysics, School of Medicine VCU. The F-20 is a Transmission Electron Microscope (TEM) that operates at 200kV and uses a Field Emission Gun (FEG) for electron emission. The final images are obtained using a CCD camera. The finer details about the various image parameters are given in the table below.

Dataset	RyR1 with Mg^{2+}	RyR2 with Amphipol
Number of CCD images	878	1200
Number of particles	10,645	25,731
Pixel size	2.33Å	2.33Å
Magnification	64,378X	64,378X
CCD Camera	Gatan Ultrascan 4000	Gatan Ultrascan 4000

Table 1: Comparison between RyR1 and RyR2 datasets

The buffer conditions that exist during the sample preparation of the two datasets are different due to the nature of the protein as well as the condition of the channel desired (i.e. whether we need the channel stable in the open or closed state). RyR1 and RyR2 are both membrane proteins and require to the removed from their normal environment in the membrane. We use detergents in order to prevent the proteins from precipitating. Detergents also reduce the surface tension of water which allows the water to form a thin and evenly distributed layer just before it freezes.

10.1 Results of Reconstruction of RyR1 with Mg^{2+}

We used 3-[(3-cholamidopropyl)dimethylammonio]-1-propanesulfonate(CHAPS) in conjunction with Mg^{2+} and the lack of Ca^{2+} to keep the channel in the closed state. Detergent is used for solubilization of the protein. As mentioned earlier the RyR1 with Mg^{2+} represents the physiologically closed state of the RyR. To accurately represent the physiological state an ATP analogue was used. ATP is a known activator of the RyR1 (as mentioned earlier) and keeps it in an open state when it used alone the combined actions of Mg^{2+} and ATP keep the channel in the physiologically closed state. Addition of lipids was not required during the preparation of the RyR1.

Search loops for run in FREALIGN to find the accurate positions of the particles with respect to the reference structure. Once the reconstructions of the RyR1 with Mg^{2+} were achieved, FSC plots were plotted in order to follow the resolution of the reconstruction.

We started the reconstruction process in the search mode or mode 4 of FREALIGN. This was continued for ten iterations, so that the resulting reconstruction is accurate and the most of the particles have found their positions. The first iteration of search yielded an FSC (0.5) of 25.2Å. After completing search, we start mode 1 also known as refinement. During the refinement stages I optimized parameters so as to achieve the best resolution. In order to do this I carried

out refinement in several separate directories using the final loop of the search mode as a common starting point. This was done so that an objective and unbiased decision could be made regarding which reconstruction is improving in terms of resolution. I optimized the values of PBC (which is a weighting value that increases the weighting on the high frequency components of a volume in Fourier space). Next I optimized the number of particles that are used in the reconstruction process using a similar process as the optimization carried out for the PBC. The Results of this optimization is shown .The refinement process was then continued using the optimized reconstructions.

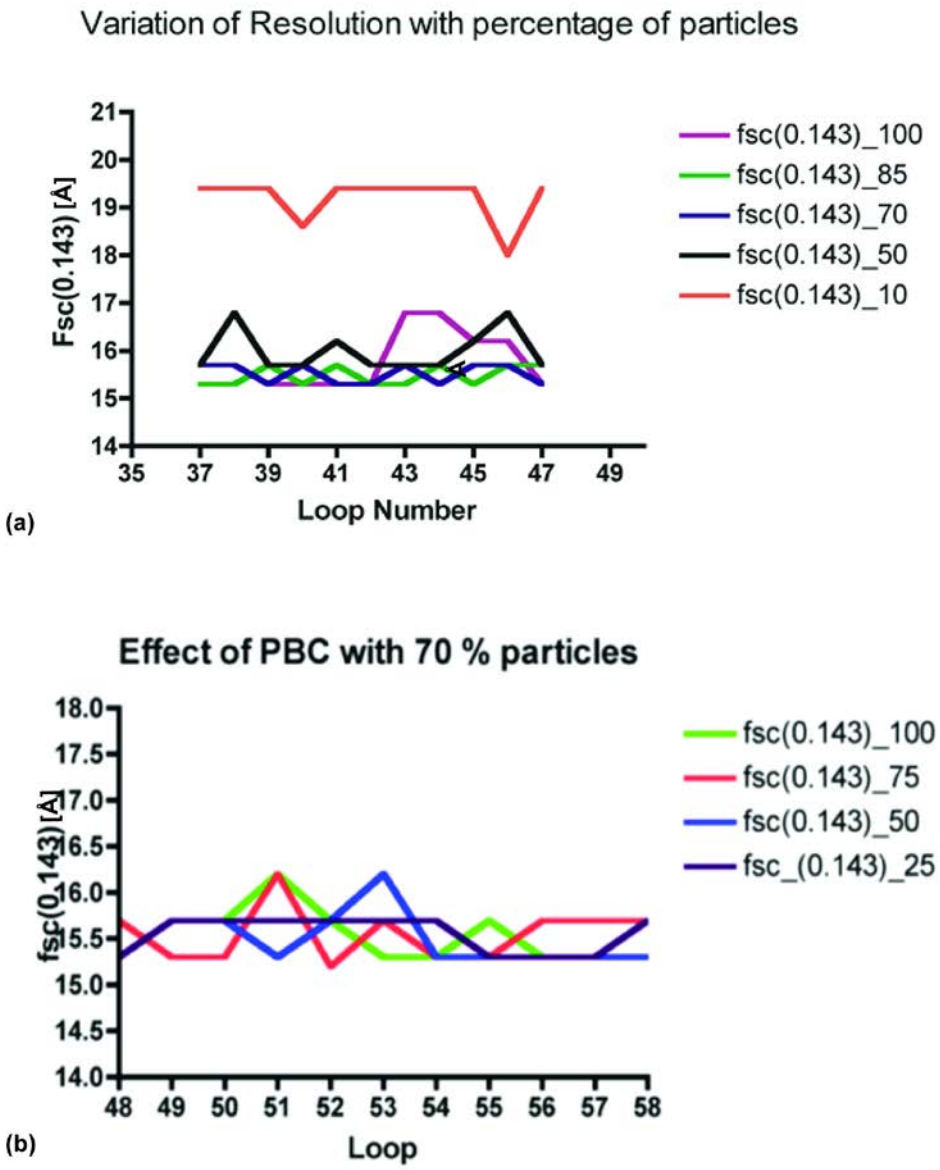

Figure 26 : Optimization of PBC values for Mg^{2+} dataset

Figure (a) shows the optimization of the threshold parameter and figure (b) shows the optimization of PBC value for the RyR1 with Mg^{2+}

PBC value of 50 gives a constantly low value of FSC (0.143) followed by PBC value of 75. Overall the variation in the resolution due to change in PBC had a minor effect on the resolution.

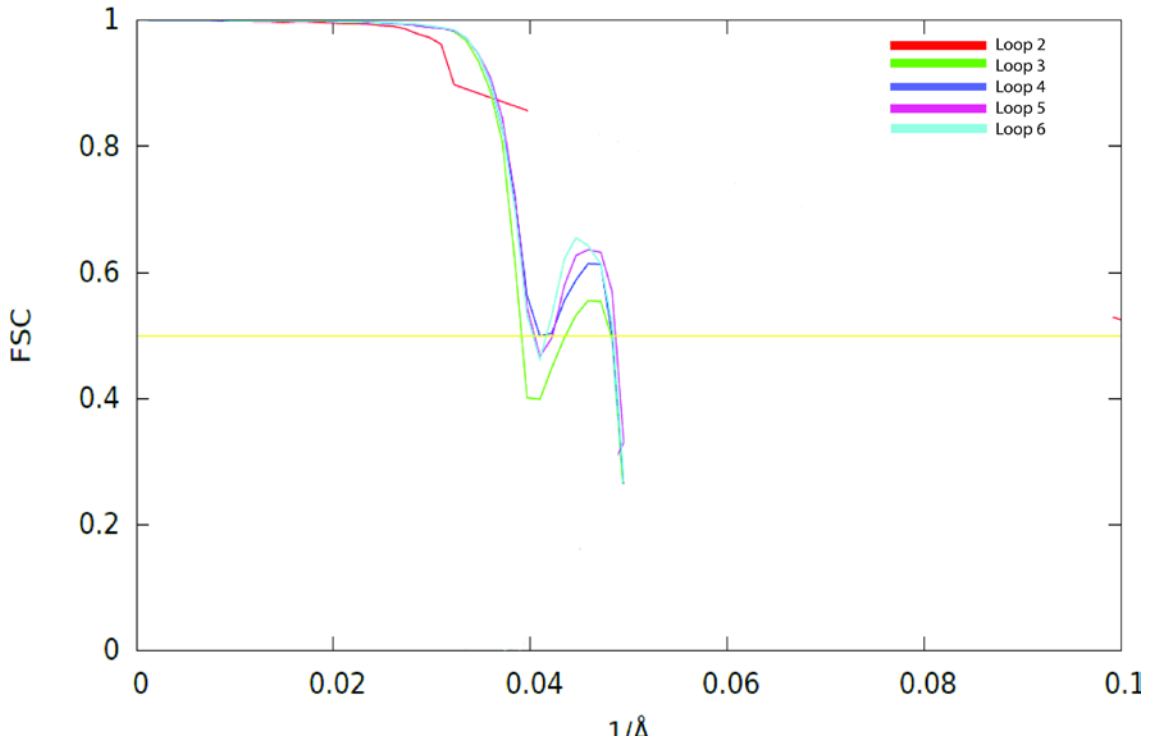

Figure 27: Initial loops of RyR1 with Mg^{2+} in “search” mode”

Loop3 had an FSC (0.5) 25.2Å .Loop 6 has an FSC (0.5) of 24.4Å

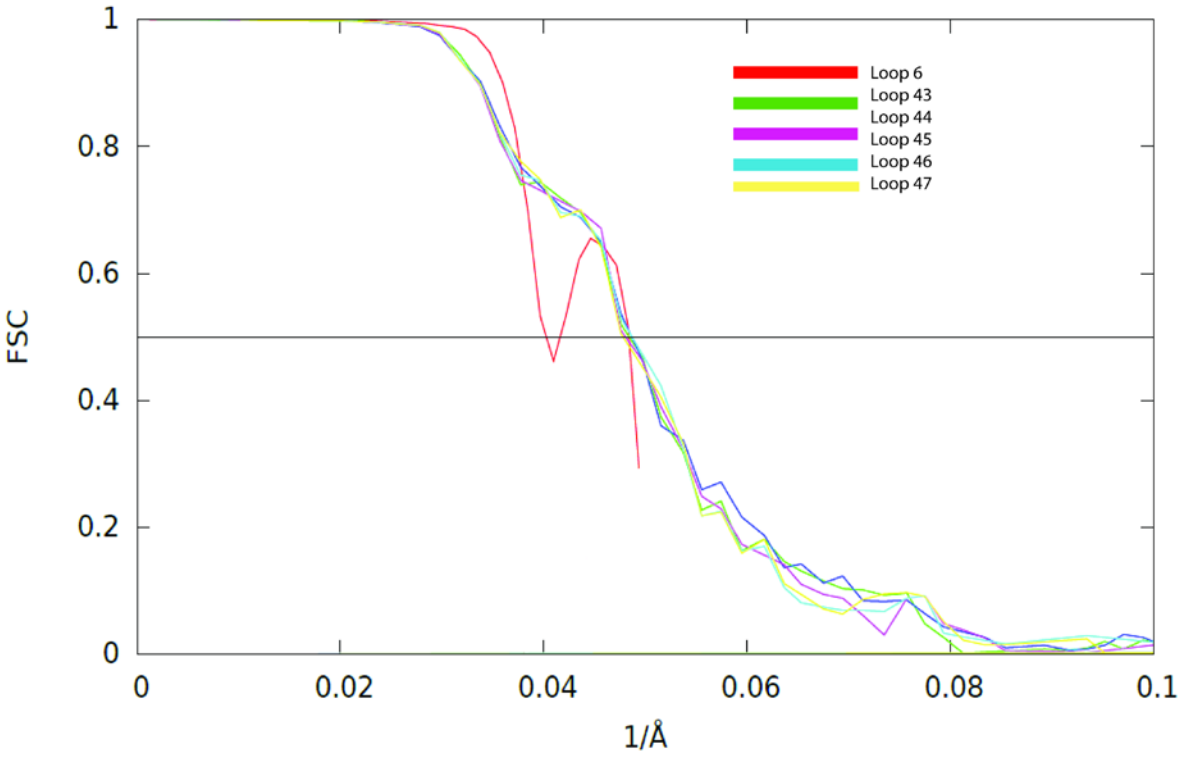

Figure 28: TM final loops of Mg^{2+} reconstruction

This graph shows the FSC plots of the loops 43 to 47 which were the final loops of the Mg^{2+} reconstruction using the complete structure. An FSC (0.5) of 20.1 Å and a FSC (0.143) of 15.7 Å were achieved. Loop 6 is shown to show the progress made

Visualization of the sectioned side views in Chimera showed a lot of density present in the TM domain. In addition it is known that the clamp domains move significantly during the closing process as established by Samso et al [77]. From a reconstruction perspective structural heterogeneity is a significant challenge in reconstructions in general [88-93]. We believe that

the movement of the clamps was causing significant misalignment of a small percentage of particles limiting our achieved resolution.

Hence, we decided to direct FREALIGN to focus more on the TM domain. The TM domain has a lot of density and is more or less stable during the gating process. The focusing was done by reducing the radius of the spherical mask which is a FREALIGN parameter. This parameter controls the radius of the circle that's in the programs field of view. The FSC graph shown below shows that there was a significant increase in the FSC (0.5) resolution as a consequence of this reduction in the radius parameter.

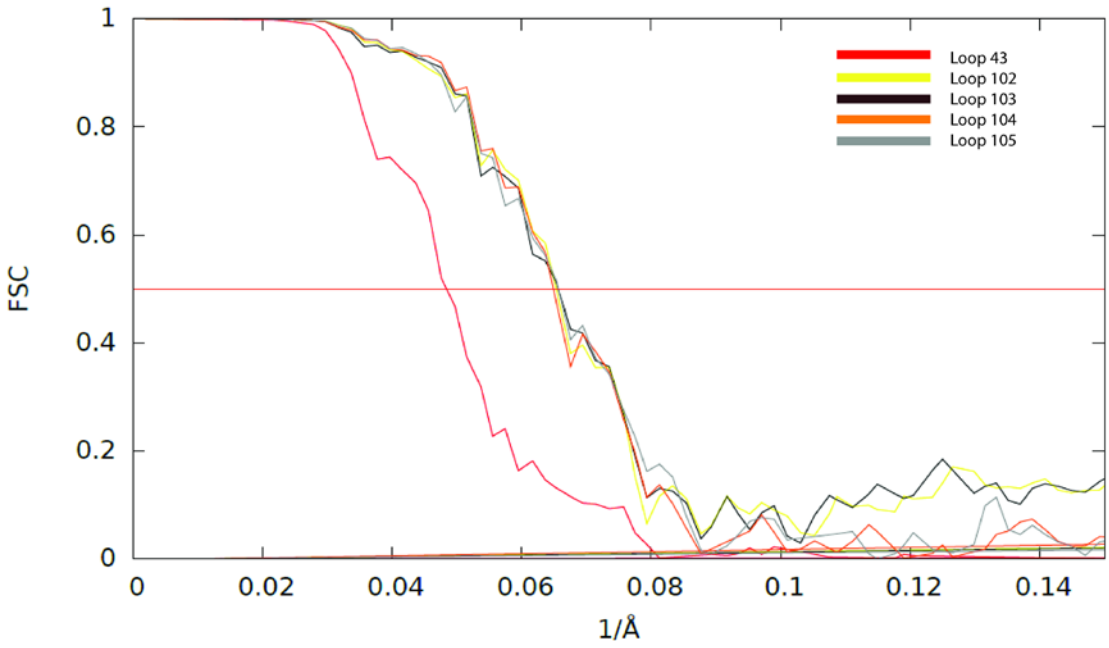

Figure 29: The loops for the reconstruction of the Mg^{2}+ transmembrane

The FSC (0.143) value achieved was 12.6Å. The reconstruction consistently returned this value for subsequent attempts which ratifies it as a stable final value. Loop 43 is shown to compare FSC curve before reduction in mask size

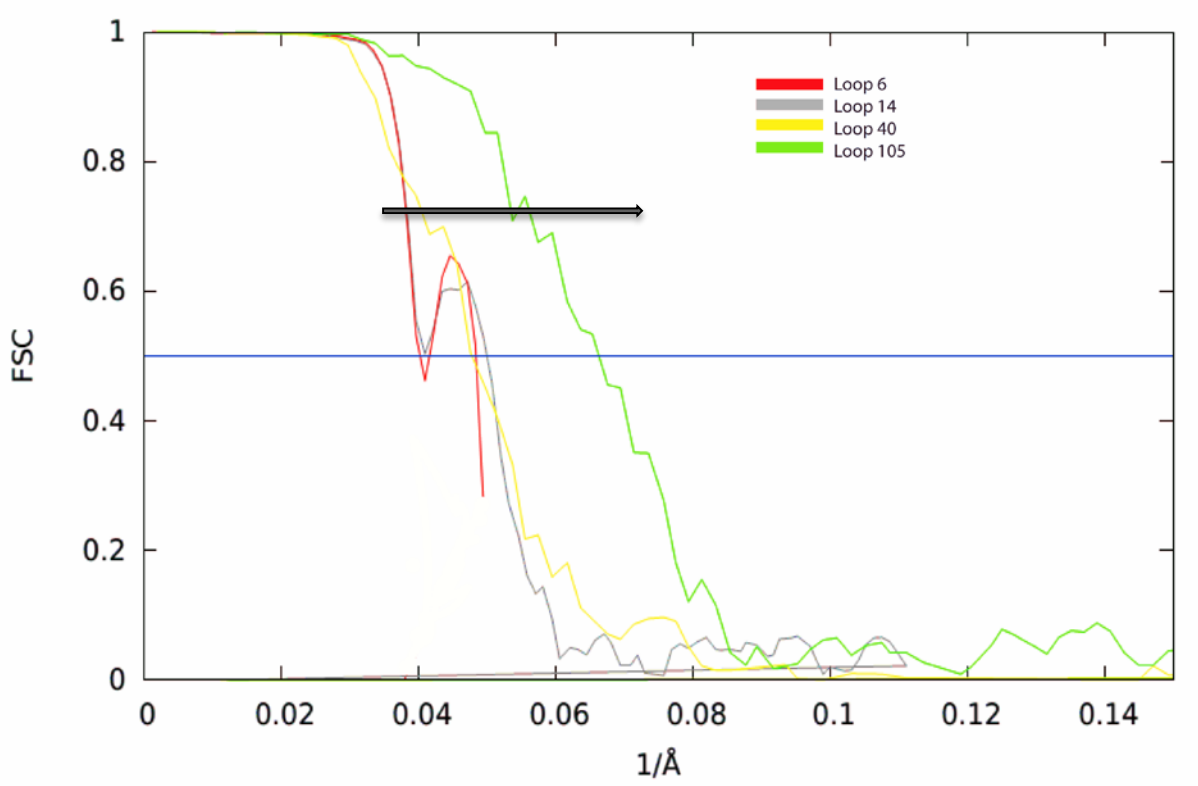

Figure 30: Summary of Mg^{2+} reconstruction

This is a summary graph showing how the reconstruction of the RyR1 with Mg^{2+} progressed. The arrowhead is pointed in the direction of a decrease in the FSC (0.5) value. Since the X axis in this graph is the reciprocal of resolution.

In conclusion ,the resolution of the structure achieved is commendable considering that the closed structures of the RyR1 without the presence of Mg^{2+} or ATP have reached ~10 Å resolution [77, 94]. Most RyR1 reconstructions have resolutions ~30Å.

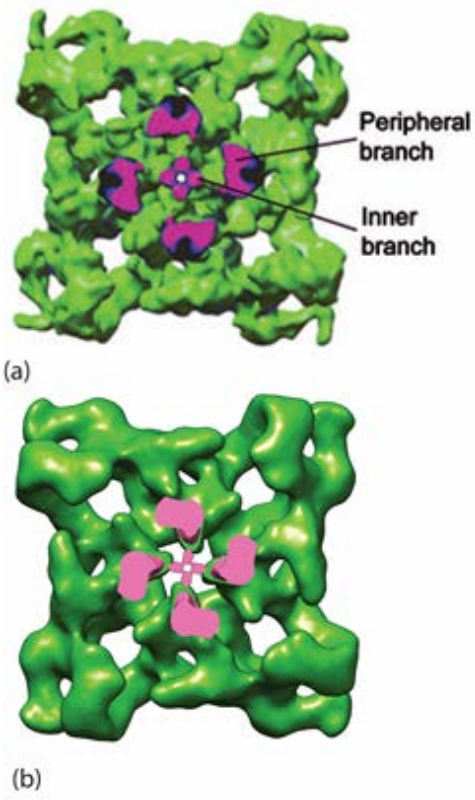

Figure 31: RyR1 with Mg^{2+} SR View

In the figure is a comparison between 2 reconstructions of RyR1.Panel (a) is RyR1 at 10Å resolution obtained by Samso et al [77]. Panel (b) is RyR1 with Mg^{2+} under the physiologically closed state. Features like the peripheral and inner branches are clearly visible.

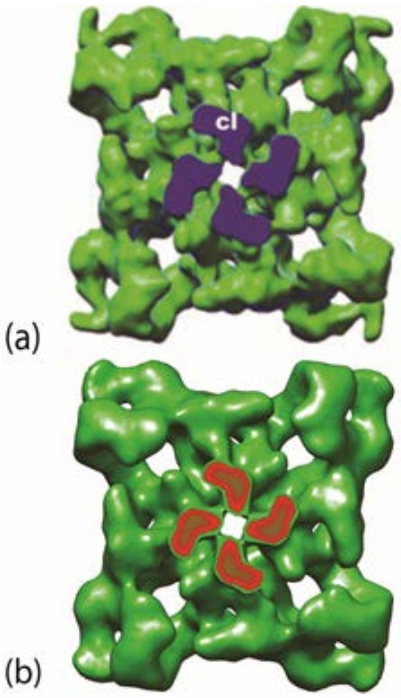

Figure 32 SR view of Mg^{2+}

The figure (a) is RyR1 with EGTA by Samso et al [77]. Figure (b) compares the RyR1 with Mg^{2+} to the structure in (a) so as to show the presence of column structures marked as c1. We see that similar columns are present in the panel (b) and are shown in red.

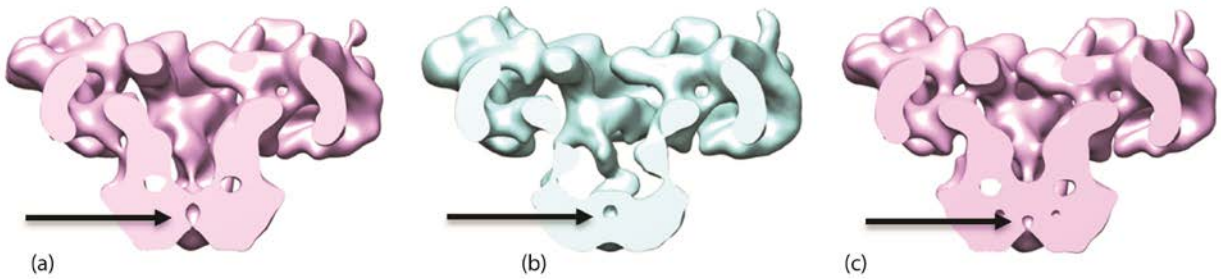

Figure 33: Comparison of resulting Reconstructions under different buffer conditions

The figure is a comparison of the RyR1 in its open, closed in the presence of Mg^{2+} and closed in the presence of EGTA (No $Mg^{2+}$is present).

The above figure shows 3 reconstructions of RyR1 which are cut by a sectioning plane that is parallel to the 4 fold axis as seen from the side view. As can be clearly seen the diameter of the central cavity is maximum in the open state shown in panel (a). The structure representing the closed state of the RyR1 in the presence of Mg^{2+} has a central cavity diameter that is in between the open and the closed. This reconstruction can be seen in panel (b).

As mentioned earlier ATP is a known activator of the RyR1 channel. Hence it would have the tendency to open the channel. Since the RyR1 with Mg^{2+} has ATP present (so as to closely resemble physiological conditions) the diameter of the central cavity has a diameter which is intermediate between the RyR1 in the open state and the RyR1 in the closed state (in the absence of Mg^{2+}). This can possibly be explained on the basis of the combined effects of Mg^{2+}

and ATP on the channel. Mg^{2+} inhibits the channel and ATP activates it leading to this intermediate closed state.

The closed structure produced in the presence of EGTA is low pass filtered for better visualization of the central cavity. Similar low pass filtering is also done for the open state reconstruction so that the three are comparable. Visualization of these reconstructions serves as a cross validation tool since the reconstruction obtained in this study is comparable to similar structures at higher resolution

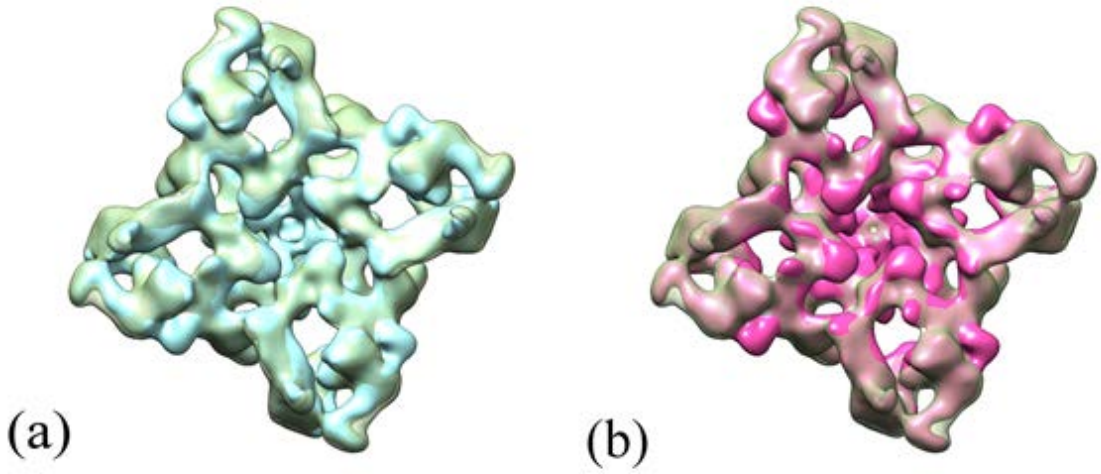

Figure 34: T tubule view of closed and open states compared with closed with Mg^{2+}

Panel (a) compares the RyR1 in closed state (with EGTA and without Mg^{2+} and ATP) in light blue with the closed state with Mg^{2+}, ATP and EGTA present (shown in light green).

Panel (b) compares the open state of RyR1 (with Ca^{2+} and PCB95) in pink with a RyR with Mg^{2+} reconstruction similar to that shown in panel (a).

Once the reconstruction of the RyR1 with Mg^{2+} was obtained we fitted this reconstruction to the closed state of the RyR containing both FKBP12 and EGTA using UCSF Chimera. This map was determined previously by Samso et al [77] (EMDB Accession number 1607) having a resolution of 10.3Å at the FSC (0.143) cutoff. The fitting procedure provided us a very high cross-correlation of 0.992 as we had expected. The figure shows the different mass distributions in the RyR1 .Panel (a) compares the closed state with EGTA and without Mg^{2+} obtained by Samso et al[77] (in light blue) with the RyR1 with Mg^{2+}(in light green) . There are subtle changes in the density distributions that suggest that RyR1 with EGTA is the tighter closed state among the two. In panel (b) we show a similar view as in panel (a), but using different reconstructions. We now compare the RyR1 (with Mg^{2+}) to the RyR1 without EGTA or Mg^{2+} (the native open state in the presence of activator Ca^{2+}) given by the structure in pink. When comparing the two structures it is evident with the pink structure showing the initial appearance of the pore that is the open when compared to the reconstruction in the presence of Mg^{2+}.

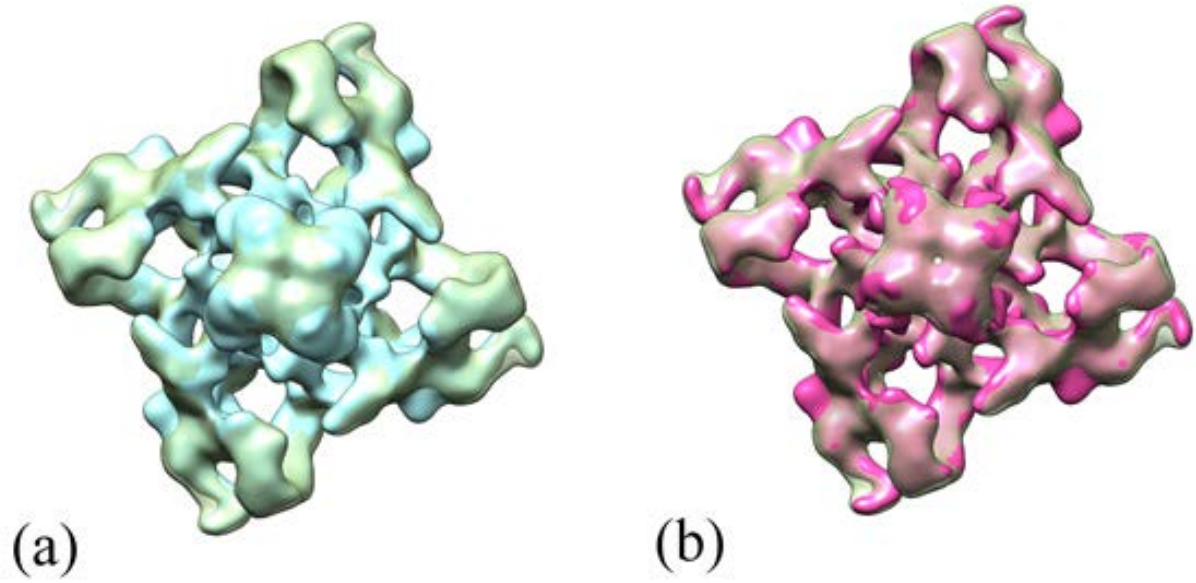

Figure 35 : SR view of closed and open states compared with closed with Mg^{2+}

Panel (a) compares the RyR1 in closed state (with EGTA and without Mg^{2+} and ATP) in light blue with the closed state with Mg^{2+} , ATP and EGTA present (shown in light green). Panel (b) compares the open state of RyR1 (with Ca^{2+} and PCB95) in pink with a RyR with Mg^{2+} reconstruction similar to that shown in panel (a).

The above figure compares RyR1 with Mg^{2+} (in light green) with the reconstruction of RyR1 in the presence of Mg^{2+} in panel (a). Panel (b) is a similar view as panel (a), however it compares the RyR1 with Mg^{2+} reconstruction with the open state RyR1 without Mg^{2+} or EGTA.(the native open state is shown in pink) . The arrangement of densities in panel (a) show that RyR1 with EGTA is the more closed state when compared with the reconstruction

containing Mg^{2+}. One would notice more changes in the densities in panel (b) since the differences between the RyR1 with Mg^{2+} and the open RyR1 are greater.

The RyR1 in the native closed state has EGTA present which has a known inhibitory effect on the RyR1 channel and keeps the channel closed. Though Mg^{2+} is an inhibitor and tends to also keep the RyR1 also closed the presence of ATP which is a known activator of RyR1 makes the

RyR1 with Mg^{2+} less closed than the RyR1 with EGTA and without Mg^{2+} or ATP present

In the case of the comparison between the open state of RyR1 (in the presence of PCB 95 and Ca^{2+}) and the RyR1 closed state with Mg^{2+} present we observe a noticeable difference between the reconstructions. The RyR1 with $Mg^{2+,}$ though being a less closed state is clearly seen to be closer to the RyR1 in closed state than the open.

The overall motion of opening (from closed state with EGTA or the closed state with Mg^{2+} to the opened state) is best described as “tilting” and an upward and outward movement of the corners or the clamp domains moving away from the T-tubule and towards the SR.

Docking of N-terminal Domains of Skeletal RyR1 and Mutation Analysis

In total 300 disease mutations have been identified in the RyR1 and have found to be associated with diseases like Malignant Hyperthermia (MH) and Central Core Disease. The N-terminus is a known disease hotspot. It consists of 3 domains named A, B and C. Several interactions are believed to occur, especially during the closing of the channel. We wanted to analyze what would happen if these atomic structures are docked into our 3Dmap of RyR1 with Mg^{2+}

To do this we started off by fitting the crystal of the N-terminus atomic structures (PDB ID: 2XOA) to the structure of the RyR1 in the closed state (in the presence of EGTA and CHAPS).Aligning the atomic structure of the N-terminal domains to the RyR1 in closed state 3D map (obtained by Samso et al [77]) was done so that the fitting of these structures was accurate. Fitting of the N terminus domain to the 10.2 Å map by Samso et al [77] was also carried out in another study by Petegem et al.[95] with similar results. He used a program called Situs [96] in order to dock the N terminus region to maps having EMDB accession numbers 1275[94],5014[77] and 1274[97] and found that they docked at the same position around the 4 –fold symmetry axis. We then fit the atomic N-terminus structures to our map of RyR1 with Mg^{2+} and achieved similar results as those obtained by Situs.

Finally using the atomic specification instruction set (which is also present in Chimera) we marked the mutations caused by Central Core Disease and Malignant Hyperthermia (MH) using data from several studies [95, 98-100]. We particularly focus on two important residues, the ones marked in blue correspond to R321 and R329. The side chain containing R329 is flexible and can come within the 3.5Å of R321 [101]. When the B domains come closer to each other for example, during the closed state these mutations and the domain interactions become important.

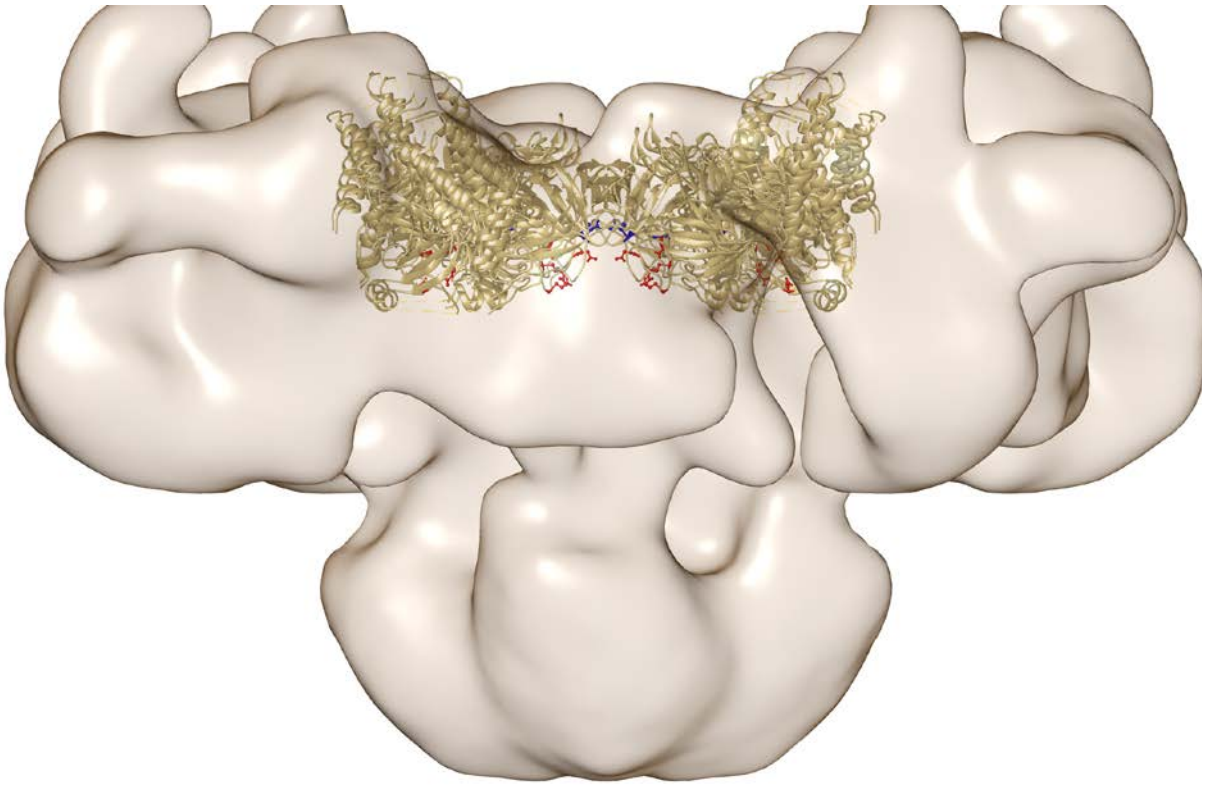

Figure 36 Docking of atomic structures into 3D map and mutation analysis

Figure showing the side view with the N-terminus docked atomic structures. Highlighted in blue are R321 and R329. The other mutations that occur at interface 1 are highlighted in red.

The mutations which are of interest are R321 and R239 and are marked in blue. The other mutations marked in red are also mutations that occur at the interface 1.

Interface 1 is formed between neighboring A and B subunits. When the channel is closed these domains interact as shown by Petegem et al [95] . The R321 and R329 which are marked in blue come within a 3.5Å distance of each other and hence are important when considering the interaction of the domains during the closing of the channel.

10.2 Comparing RyR1 with RyR2 under Different Levels of Noise

The second goal of my work was to analyze the problem of noise bias which as explained in the introductory section on this topic is the alignment of noise into the reference structure leading to physiologically implausible results.

In order to do this I compared 2 Datasets .The RyR1 with Mg^{2+} in the presence of CHAPS with the RyR2 in the presence of CHAPS (0.25%) and Amphipol (0.3%) (Both of which are detergents). By its nature Amphipol replaces CHAPS leaving only the RyR2 with Amphipol. Similar processing and optimization steps were carried out for the RyR2 so that the results would be comparable. The optimization of PBC (a resolution dependent weighting value) and threshold are shown in the figures below.

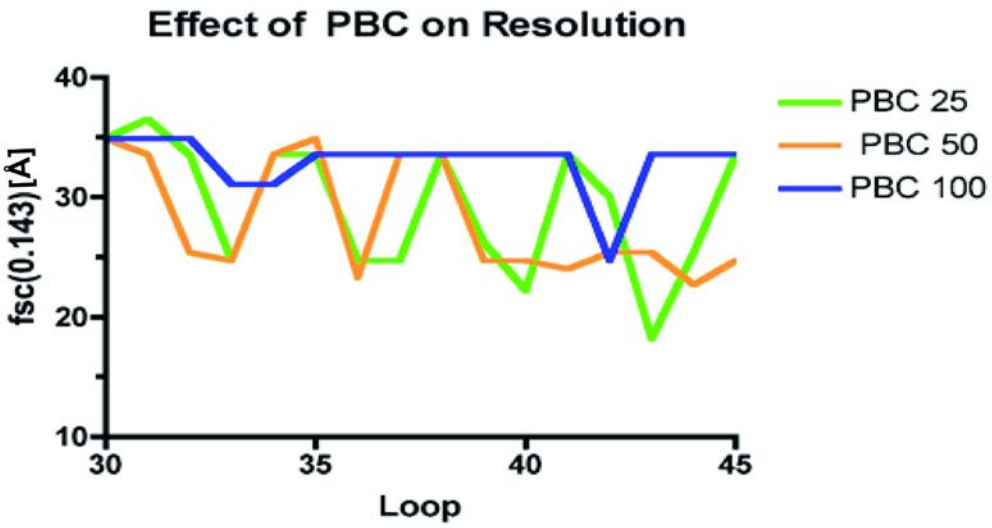

Figure 37:Effect of PBC on Resolution with Changed Mask Radius

The following graph shows the variation in the resolution at an FSC of 0.143 when PBC was changed for the three cases where PBC=100, 50, and 25. The outer mask radius was changed from 190Å to 180Å. PBC 50 was chosen as the best since it showed consistently lower fsc (0.143) values which implicated higher resolution.

In comparison to the PBC optimization of the Mg^{2+} dataset the RyR2 was difficult to optimize possibly also suggesting high levels of noise in the data

Shown below is the initial search loops of the RyR2 with Amphipol dataset. For the loops shown in the figure the FSC (0.5) was 36.5Å and the FSC (0.143) was at 34.9Å.We see that loop 6 is a significant improvement from loop 2.

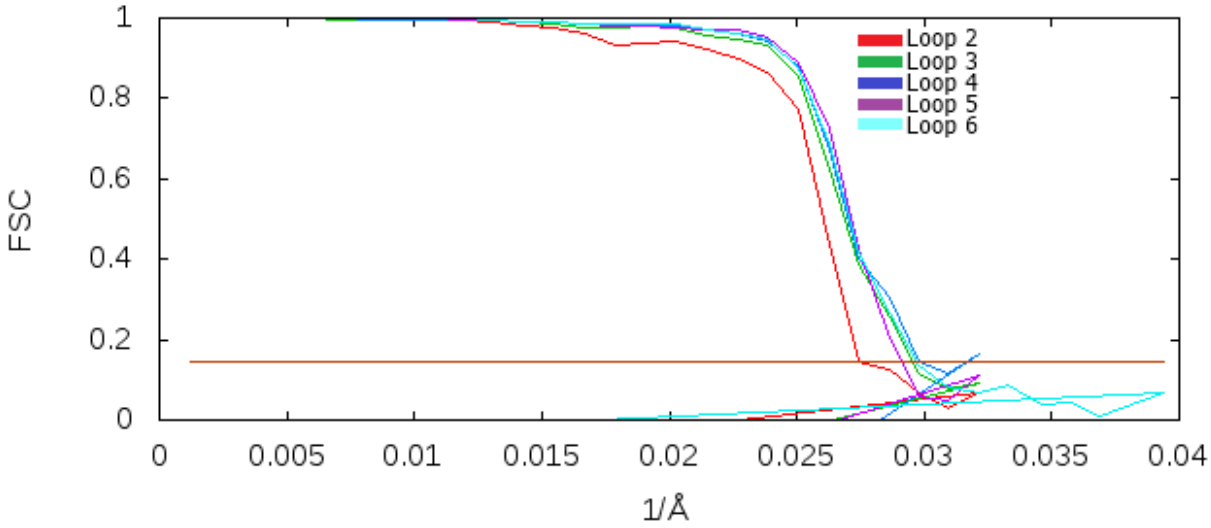

Figure 38: Initial Loops of RyR2 dataset

The figure shows the FSC curves of loops 2 to 6 of the RyR2 Dataset

Search or mode 4 of FREALIGN operation was carried for 20 loops to achieve a stable structure .The structure was then refined using the mode 1 of FREALIGN operation. Optimization of the various reconstruction parameters was carried out similar to the RyR1 dataset and the optimized reconstructions were further processed.

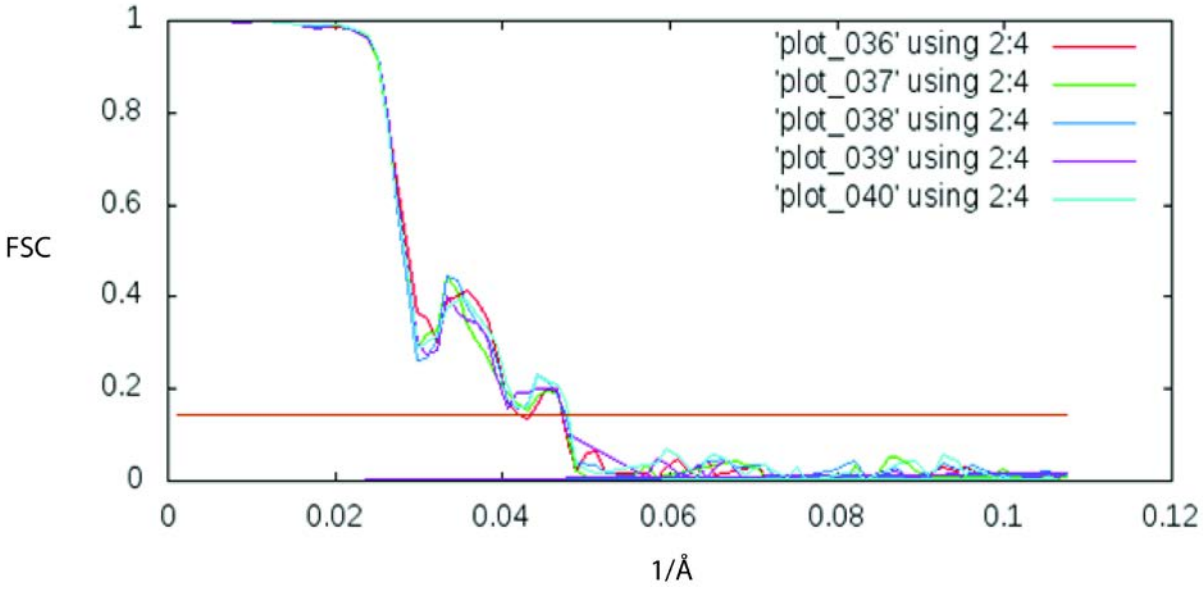

Figure 39: Progression of RyR2 dataset loops 36-40

The Figure shows that the FSC (0.5) reduced to 34.9Å and the FSC (0.143) was at 20.2Å

.

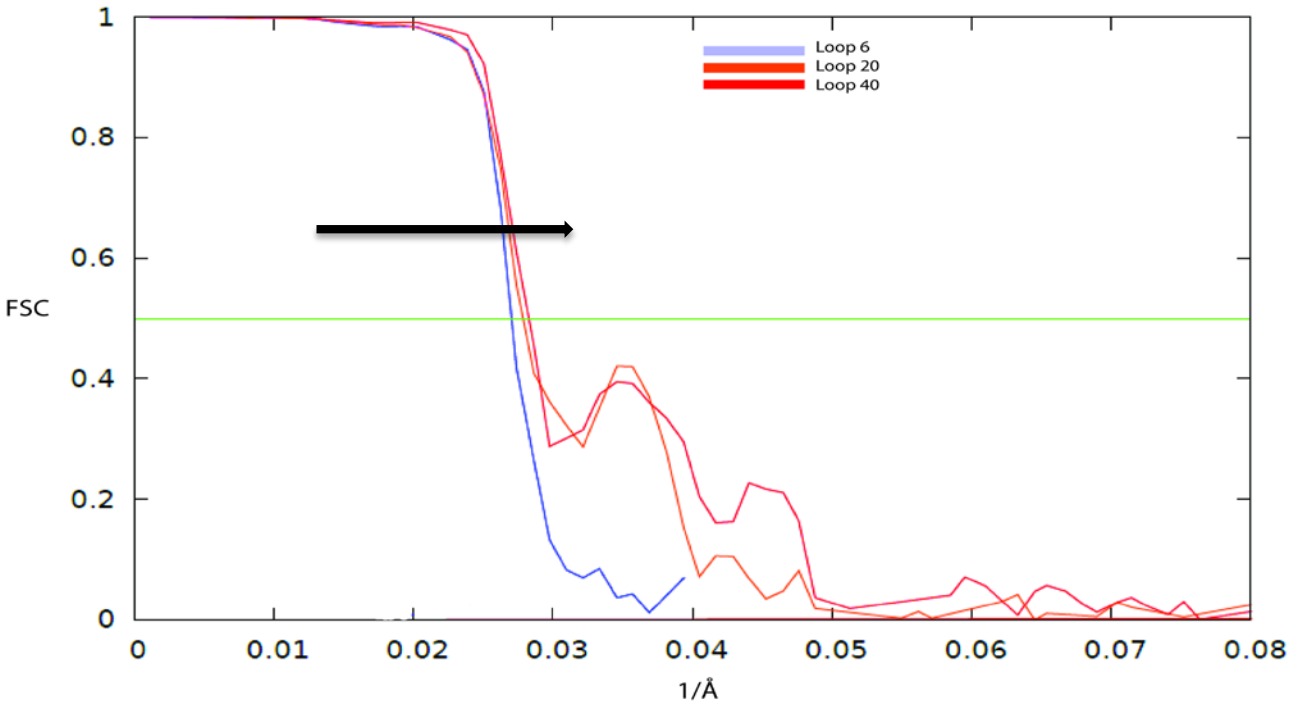

Figure 40 Summary for the RyR2 Image Processing

The figure serves as a summary graph for all the image processing done for the RyR2 dataset in the presence of Amphipol. The arrow is drawn in the direction of decreasing FSC (0.5).

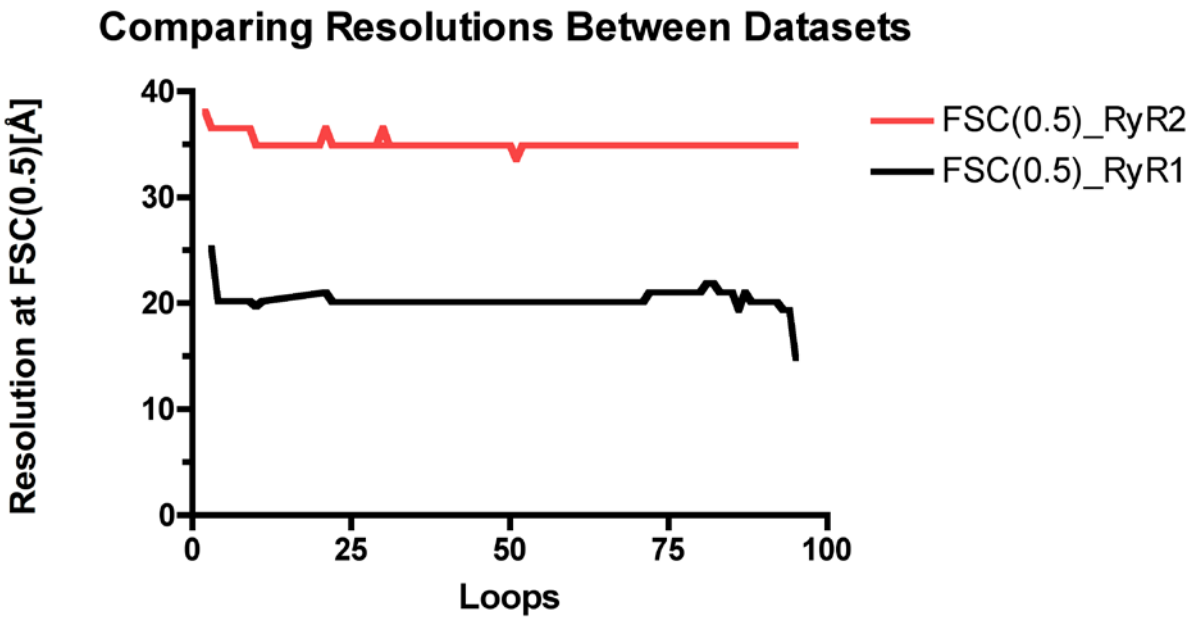

Figure 41: Overall comparison between Datasets

This is a summary graph for both RyR1 and RyR2 datasets, the arrow shows the point at which only the TM domain was reconstructed.

Dataset	RyR1 with Mg^2	RyR2 with Amphipol
Number of Particles	10645	25731
FSC(0.5)	20.1Å*	34.9Å
FSC(0.143)	15.7Å*	20.5Å

Table 2: Resolution comparison of RyR1 v/s RyR2 reconstructions.

*The FSC (0.143) value is 15.7 Å for the complete structure. Since the RyR2 is a complete structure this is a fair comparison. However a resolution of 12.6 Å was achieved for the transmembrane domain

The figure above shows the results from the two datasets in order to gain better perspective of how the reconstructions progressed in each situation. The resolution values at the two cutoffs of FSC (0.5) and FSC (0.143) are furnished in the table. For a fair comparison we compared the structure of the RyR1 (and not just the TM domain) with the complete structure of the RyR2.

To better visualize the problem of alignment of noise to the structures we observed the RyR2 structures in Chimera. The results of this visualization is shown below.

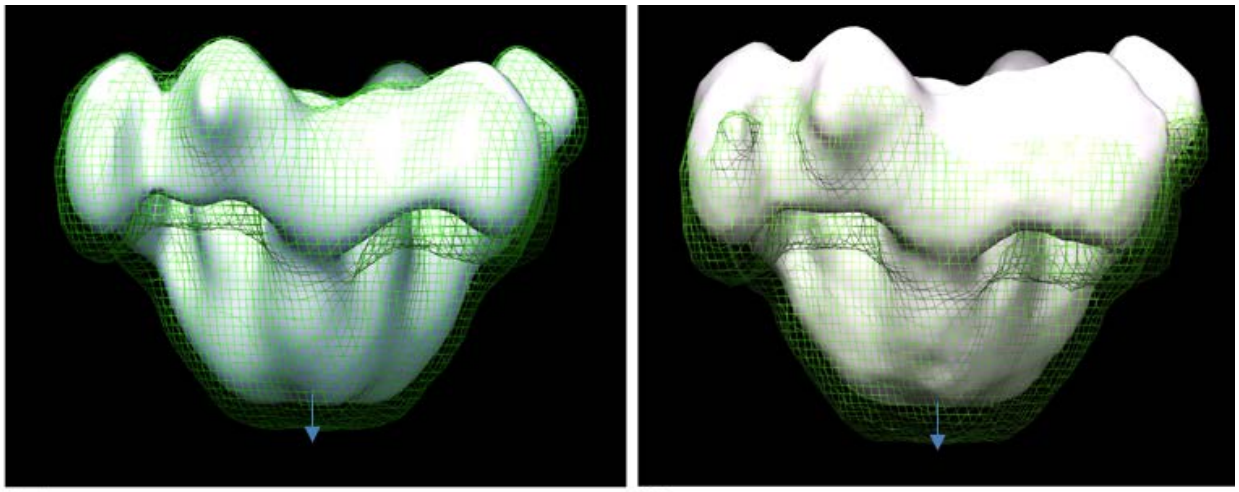

Figure 42: RyR2 reconstruction comparison

RyR2 comparison between the reconstructions at loop 6 v/s loop 40 in panel (a) and panel shows loop 6 v/s loop 40. Panel (b) on the right shows the comparison between loop 40 and loop 94 of the RyR2 reconstruction and how the TM domain is elongated

As can be seen in table 2 above we used two datasets in order to analyze the problem of noise bias under different levels of noise. The RyR2 with Amphipol dataset contained nearly 2.5 times the number of particles when compared to the RyR1 with Mg^{2+} dataset. However, the fsc (0.5) resolution obtained by the RyR1 dataset was significantly better. Though the RyR2 had an apparent resolution of FSC (0.143) =20.5Å the transmembrane domain was elongated beyond plausible limits. In order to validate our findings we compared the classes from the RyR2 dataset and the 3D reconstructions that were achieved. The observed classes did not represent the 3D reconstruction in the transmembrane domain. Thus we were clearly able to conclude that the elongation of the TM domain is indeed due to noise bias.

RyR2 found predominantly in the heart is a membrane protein. The purification of which involves the solubilization of proteins and lipids using a detergent (Amphipol) as well as the addition of additional lipids during its purification. Amphipol is a detergent that was expected to increase the contrast of the particles. However the detergent added a lot of noise to the particles hindering the 3D reconstruction process. This is what we believed to have caused the problem of noise bias. The purification of RyR1 on the other hand is comparatively straight forward and doesn't require the addition of lipids.

In order to compare qualitatively the noise that was present in the RyR1 dataset (with Mg^{2+}) with the noise present in case of the RyR2 dataset with Amphipol we use figure 43. The figure shows the reconstruction of the ribosome under different levels of noise by Radermacher et al[2].These model datasets that were created under different conditions of tilt. The numbers correspond to the increasing amount of noise.

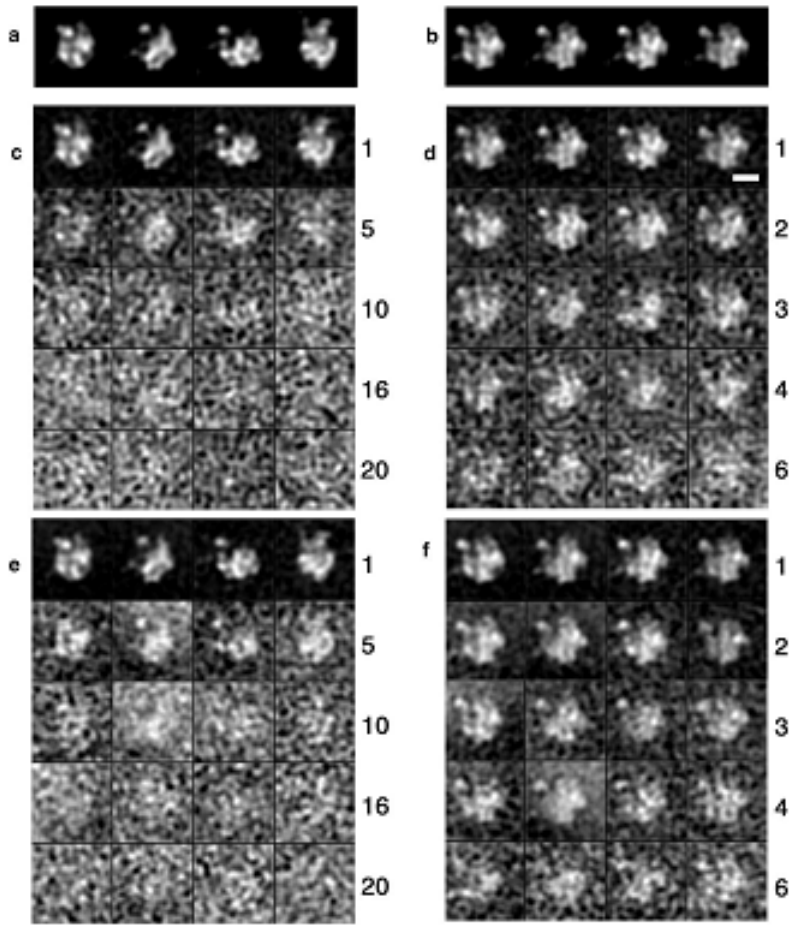

Figure 43: Projections with Increasing Noise

Model datasets obtained by tilting the 3D reconstruction of the ribosome by Radermacher et al [2]. Different tilt conditions are used as follows: high (a) and similar, low (b) tilts. (c)–(f).Gaussian noise is added(increased) in order of the increasing numbers.

Seen in the figure below is a montage of images that from the RyR1 dataset with Mg^{2+} shown in panel (a) and the RyR2 dataset, which is shown in panel (b). These were created in SPIDER and viewed through WEB.

We saw that the RyR2 classes were similar to the noise level observed in the high-tilt condition observed in panel c 10. In comparison the classes of the RyR1 dataset with Mg^{2+} and CHAPS is similar to the classes shown in panel d 2. There is an easily observable difference in the noise levels of the two classes as seen in the figure below

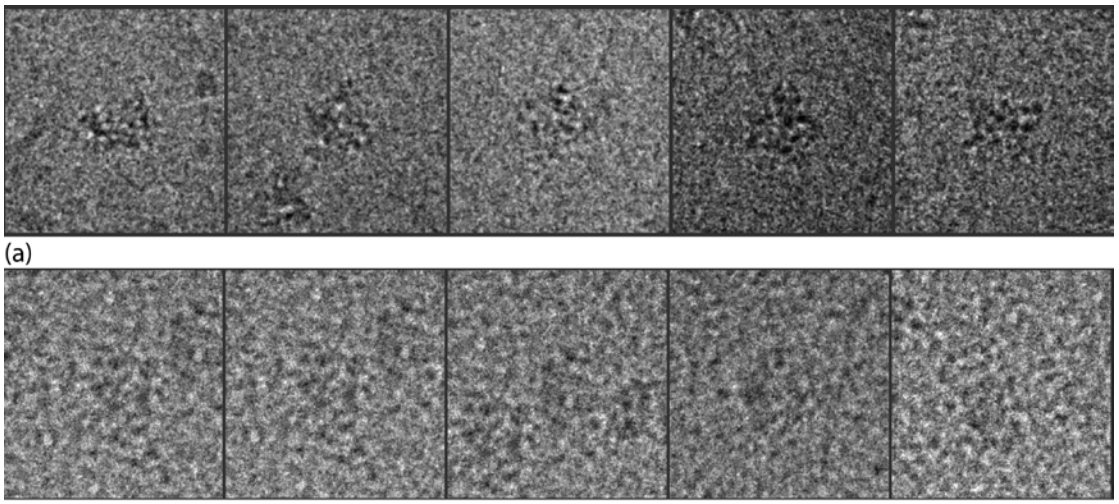

Figure 44: Comparison of Noise levels in RyR1 v/s RyR2 dataset

We observe clear RyR's in panel (a) with boundaries that are easily distinguishable as separate from the background noise. In comparison it is much harder to distinguish the

boundaries in panel (b) due to the high level of noise. This clearly demonstrates the difference in the amount of noise present in the two datasets.

11. Conclusion and Future Work

The reconstruction of the RyR1 in the presence of Mg^{2+} was successfully obtained with an FSC (0.143) =15.7Å for the complete structure, with the transmembrane domain achieving a FSC (0.143) resolution of 12.6Å in a physiologically closed state. The reconstructions of the RyR1 in the open and closed state which were achieved earlier by Samso et al were the foundations of these findings. Through the comparison of the physiologically closed state in the presence of CHAPS, Mg^{2+} and an ATP analogue we showed that this physiologically closed state is closer to the closed state than the open state. We also showed that the RyR1 in the physiologically closed state is not as closed when compared to the closed state without Mg^{2+}.

Since we are always striving for better resolution in the cryo-EM field our efforts will focus on attaining higher resolution. Higher resolution 3D maps will help to better understand the structure and how changes in the structure relate to function. In the case of RyR1 with Mg^{2+} we hope to use a direct electron detector (instead of a CCD) which should significantly increase the quality of images acquired.

Studying the RyR2 under different levels of noise demonstrated the problem of noise bias that is present in cryo-EM today. The utility and need of different validation techniques other than just Fourier shell correlation curves was greatly highlighted.

Henderson et al [83] outlines several pragmatic guidelines in order to tackle the problem of noise bias . He suggests obtaining a few images at large defocus and high exposure levels. High exposure of 80, 100, or even up to 140 el/$Å^2$ is very likely to cause radiation damage in the sample though avoids the "Einstein from Noise" pitfall which is seen in previous sections. This is possible remedy however it must be noted that a balance must be struck between contrast and resolution.

Sample preparation with different concentrations of Amphipol in order to get the least noise is one possible remedial direction to tackle the level of noise in the RyR2 data. Removal of the residual CHAPS after it has been substituted by Amphipol is another possible remedy to reduce the amount of noise causing detergents in the preparation.

Calculation of resolution from "gold standard" FSC curves gives a realistic resolution value of the reconstruction. FREALIGN calculates the FSC values based on two half datasets. One dataset contains even and the other dataset contains odd particles. If high noise is present in one of these datasets it can bias the calculation of FSC. In order to prevent this we can use an

alternative method to validate the reconstruction.. This is done so that the half reconstructions are free from any false correlation.

Bibliography

1. Dr.Steve.B.Howell, *Basics of Charge Couple Devices* National Optical Astronomy Observatory.
2. Radermacher, M., et al., *Three-dimensional reconstruction from a single-exposure, random conical tilt series applied to the 50S ribosomal subunit of Escherichia coli.* J Microsc, 1987. **146**(Pt 2): p. 113-36.
3. Kettlun, C., et al., *Unitary Ca2+ current through mammalian cardiac and amphibian skeletal muscle ryanodine receptor Channels under near-physiological ionic conditions.* J Gen Physiol, 2003. **122**(4): p. 407-17.
4. Jurkat-Rott, K. and F. Lehmann-Horn, *Muscle channelopathies and critical points in functional and genetic studies.* J Clin Invest, 2005. **115**(8): p. 2000-9.
5. Rebbeck, R.T., et al., *Skeletal muscle excitation-contraction coupling: who are the dancing partners?* Int J Biochem Cell Biol, 2014. **48**: p. 28-38.
6. Dulhunty, A.F., et al., *Interactions between dihydropyridine receptors and ryanodine receptors in striated muscle.* Prog Biophys Mol Biol, 2002. **79**(1-3): p. 45-75.
7. Nakai, J., et al., *Enhanced dihydropyridine receptor channel activity in the presence of ryanodine receptor.* Nature, 1996. **380**(6569): p. 72-5.
8. Beam, K.G. and R.A. Bannister, *Looking for answers to EC coupling's persistent questions.* J Gen Physiol, 2010. **136**(1): p. 7-12.
9. Fujimoto, K., *Freeze-fracture replica electron microscopy combined with SDS digestion for cytochemical labeling of integral membrane proteins. Application to the immunogold labeling of intercellular junctional complexes.* J Cell Sci, 1995. **108 (Pt 11)**: p. 3443-9.
10. Protasi, F., et al., *Multiple regions of RyR1 mediate functional and structural interactions with alpha(1S)-dihydropyridine receptors in skeletal muscle.* Biophys J, 2002. **83**(6): p. 3230-44.
11. Schredelseker, J., et al., *Proper restoration of excitation-contraction coupling in the dihydropyridine receptor beta1-null zebrafish relaxed is an exclusive function of the beta1a subunit.* J Biol Chem, 2009. **284**(2): p. 1242-51.
12. Schredelseker, J., et al., *The beta 1a subunit is essential for the assembly of dihydropyridine-receptor arrays in skeletal muscle.* Proc Natl Acad Sci U S A, 2005. **102**(47): p. 17219-24.
13. Sheridan, D.C., et al., *Bidirectional signaling between calcium channels of skeletal muscle requires multiple direct and indirect interactions.* Proc Natl Acad Sci U S A, 2006. **103**(52): p. 19760-5.
14. Weiss, R.G., et al., *Functional analysis of the R1086H malignant hyperthermia mutation in the DHPR reveals an unexpected influence of the III-IV loop on skeletal muscle EC coupling.* Am J Physiol Cell Physiol, 2004. **287**(4): p. C1094-102.

15. Tang, W., S. Sencer, and S.L. Hamilton, *Calmodulin modulation of proteins involved in excitation-contraction coupling.* Front Biosci, 2002. **7**: p. d1583-9.
16. Cui, Y., et al., *A dihydropyridine receptor alpha1s loop region critical for skeletal muscle contraction is intrinsically unstructured and binds to a SPRY domain of the type 1 ryanodine receptor.* Int J Biochem Cell Biol, 2009. **41**(3): p. 677-86.
17. Paolini, C., et al., *Evidence for conformational coupling between two calcium channels.* Proc Natl Acad Sci U S A, 2004. **101**(34): p. 12748-52.
18. Karunasekara, Y., A.F. Dulhunty, and M.G. Casarotto, *The voltage-gated calcium-channel beta subunit: more than just an accessory.* Eur Biophys J, 2009. **39**(1): p. 75-81.
19. Chen, Y.H., et al., *Structural basis of the alpha1-beta subunit interaction of voltage-gated Ca2+ channels.* Nature, 2004. **429**(6992): p. 675-80.
20. Opatowsky, Y., et al., *Structural analysis of the voltage-dependent calcium channel beta subunit functional core and its complex with the alpha 1 interaction domain.* Neuron, 2004. **42**(3): p. 387-99.
21. Van Petegem, F., et al., *Structure of a complex between a voltage-gated calcium channel beta-subunit and an alpha-subunit domain.* Nature, 2004. **429**(6992): p. 671-5.
22. Kistner, U., C.C. Garner, and M. Linial, *Nucleotide binding by the synapse associated protein SAP90.* FEBS Lett, 1995. **359**(2-3): p. 159-63.
23. Richards, M.W., A.J. Butcher, and A.C. Dolphin, *Ca2+ channel beta-subunits: structural insights AID our understanding.* Trends Pharmacol Sci, 2004. **25**(12): p. 626-32.
24. Strube, C., et al., *Reduced Ca2+ current, charge movement, and absence of Ca2+ transients in skeletal muscle deficient in dihydropyridine receptor beta 1 subunit.* Biophys J, 1996. **71**(5): p. 2531-43.
25. Beurg, M., et al., *Involvement of the carboxy-terminus region of the dihydropyridine receptor beta1a subunit in excitation-contraction coupling of skeletal muscle.* Biophys J, 1999. **77**(6): p. 2953-67.
26. Sheridan, D.C., et al., *Involvement of a heptad repeat in the carboxyl terminus of the dihydropyridine receptor beta1a subunit in the mechanism of excitation-contraction coupling in skeletal muscle.* Biophys J, 2004. **87**(2): p. 929-42.
27. Cheng, W., et al., *Interaction between the dihydropyridine receptor Ca2+ channel beta-subunit and ryanodine receptor type 1 strengthens excitation-contraction coupling.* Proc Natl Acad Sci U S A, 2005. **102**(52): p. 19225-30.
28. Bers, D.M., *Cardiac excitation-contraction coupling.* Nature, 2002. **415**(6868): p. 198-205.
29. Peterson, B.Z., et al., *Calmodulin is the Ca2+ sensor for Ca2+ -dependent inactivation of L-type calcium channels.* Neuron, 1999. **22**(3): p. 549-58.
30. Zuhlke, R.D., et al., *Calmodulin supports both inactivation and facilitation of L-type calcium channels.* Nature, 1999. **399**(6732): p. 159-62.

31. Fabiato, A., *Calcium-induced release of calcium from the cardiac sarcoplasmic reticulum.* Am J Physiol, 1983. **245**(1): p. C1-14.
32. Cheng, H., W.J. Lederer, and M.B. Cannell, *Calcium sparks: elementary events underlying excitation-contraction coupling in heart muscle.* Science, 1993. **262**(5134): p. 740-4.
33. Zima, A.V., et al., *Ca handling during excitation-contraction coupling in heart failure.* Pflugers Arch, 2014.
34. Hanspeter, N. 1999 November 05, 2012 May 5,2014]; Available from: http://www.snaggledworks.com/em_for_dummies/.
35. Wagner, R.C. [Adaptation] [cited 2014 6/6/2014]; Available from: www.udel.edu/Biology/Wags/b617/b617.htm.
36. Frank, J., *Electron Microcopy Of Molecular Assemblies*, in *Three-Dimensional Electron Microscopy of Macromolecular Assemblies : Visualization of Biological Molecules in Their Native State*. 2006, Oxford University Press Cary, NC, USA p. 427
37. Glaeser, R.M., *Cryo-electron microscopy of biological nanostructures.* Physics Today, 2008. **61**(1): p. 48-54.
38. Nogales, E. *Introduction to Electron Microscopy*. [Webinar] 2010; Available from: http://www.youtube.com/watch?v=nkGRhYv01ag.
39. Milne, J.L., et al., *Cryo-electron microscopy--a primer for the non-microscopist.* FEBS J, 2013. **280**(1): p. 28-45.
40. Williams, D.B. and C.B. Carter, *Transmission electron microscopy : a textbook for materials science*. 1996, New York: Plenum Press. xxvii, 729 p.
41. Labelle, R.D. and S.D. Garvey, *Introduction to high performance CCD cameras.* Iciasf '95 Record - International Congress on Instrumentation in Aerospace Simulation Facilities, 1995: p. 269-273.
42. Li, Z., *Electron Microscopy (EM) Grid and carbon film Preparation for Cryo-Electron Microscopy:Cryo-EM Tutorial*. 2005, National Center of Research Resources, The National Center of Macromolecular Imaging
43. Sheehan, J. and D. Thornton, *Heterogeneity and Size Distribution of Gel-Forming Mucins*, in *Glycoprotein Methods and Protocols*, A. Corfield, Editor. 2000, Humana Press. p. 87-96.
44. ; Available from: https://javac.com.au/dv-502b-high-vacuum-deposition-platform-pr-16286.html.
45. Cabra, V.S., Montserrat, *Do's and dont's of cryo-electron microscopy: A primer on sample preparation and high quality data collection for macromolecular 3D reconstruction* 2014.
46. Sciences, E.M. 2010 3/19/10 [cited 2014 5/20/14]; Available from: http://www.emsdiasum.com/microscopy/products/brochures/2010/em-equipmentbook_update.pdf.
47. Aebi, U. and T.D. Pollard, *A glow discharge unit to render electron microscope grids and other surfaces hydrophilic.* J Electron Microsc Tech, 1987. **7**(1): p. 29-33.

48. FEI. 2014 [cited 2014 5/27/2014]; Available from: http://www.fei.com/products/vitrobot/.
49. Dubochet, J., et al., *Cryo-electron microscopy of vitrified specimens.* Q Rev Biophys, 1988. **21**(2): p. 129-228.
50. Tang, G., et al., *EMAN2: an extensible image processing suite for electron microscopy.* J Struct Biol, 2007. **157**(1): p. 38-46.
51. Frank, J., et al., *SPIDER and WEB: processing and visualization of images in 3D electron microscopy and related fields.* J Struct Biol, 1996. **116**(1): p. 190-9.
52. Wang, J., et al., *Molecular cloning and characterization of a ryanodine receptor gene in brown planthopper (BPH), Nilaparvata lugens (Stal).* Pest Manag Sci, 2014. **70**(5): p. 790-7.
53. Marziali, G., et al., *cDNA cloning reveals a tissue specific expression of alternatively spliced transcripts of the ryanodine receptor type 3 (RyR3) calcium release channel.* FEBS Lett, 1996. **394**(1): p. 76-82.
54. Nakai, J., et al., *Primary structure and functional expression from cDNA of the cardiac ryanodine receptor/calcium release channel.* FEBS Lett, 1990. **271**(1-2): p. 169-77.
55. Grigorieff, N., *FREALIGN: high-resolution refinement of single particle structures.* J Struct Biol, 2007. **157**(1): p. 117-25.
56. Pettersen, E.F., et al., *UCSF Chimera--a visualization system for exploratory research and analysis.* J Comput Chem, 2004. **25**(13): p. 1605-12.
57. Wagenknecht, T. and M. Samso, *Three-dimensional reconstruction of ryanodine receptors.* Front Biosci, 2002. **7**: p. d1464-74.
58. Radermacher, M., et al., *Cryo-electron microscopy and three-dimensional reconstruction of the calcium release channel/ryanodine receptor from skeletal muscle.* J Cell Biol, 1994. **127**(2): p. 411-23.
59. Serysheva, II, et al., *Electron cryomicroscopy and angular reconstitution used to visualize the skeletal muscle calcium release channel.* Nat Struct Biol, 1995. **2**(1): p. 18-24.
60. Orlova, E.V., et al., *Two structural configurations of the skeletal muscle calcium release channel.* Nat Struct Biol, 1996. **3**(6): p. 547-52.
61. Doyle, D.A., et al., *The structure of the potassium channel: molecular basis of K+ conduction and selectivity.* Science, 1998. **280**(5360): p. 69-77.
62. Balshaw, D., L. Gao, and G. Meissner, *Luminal loop of the ryanodine receptor: a pore-forming segment?* Proc Natl Acad Sci U S A, 1999. **96**(7): p. 3345-7.
63. Zhao, M., et al., *Molecular identification of the ryanodine receptor pore-forming segment.* J Biol Chem, 1999. **274**(37): p. 25971-4.
64. Williams, A.J., D.J. West, and R. Sitsapesan, *Light at the end of the Ca(2+)-release channel tunnel: structures and mechanisms involved in ion translocation in ryanodine receptor channels.* Q Rev Biophys, 2001. **34**(1): p. 61-104.

65. Smith, J.S., et al., *Purified ryanodine receptor from rabbit skeletal muscle is the calcium-release channel of sarcoplasmic reticulum.* J Gen Physiol, 1988. **92**(1): p. 1-26.
66. Williams, A.J., *Ion conduction and discrimination in the sarcoplasmic reticulum ryanodine receptor/calcium-release channel.* J Muscle Res Cell Motil, 1992. **13**(1): p. 7-26.
67. Sayar, K., et al., *Exploring allosteric coupling in the alpha-subunit of heterotrimeric G proteins using evolutionary and ensemble-based approaches.* BMC Struct Biol, 2008. **8**: p. 23.
68. Samso, M., T. Wagenknecht, and P.D. Allen, *Internal structure and visualization of transmembrane domains of the RyR1 calcium release channel by cryo-EM.* Nat Struct Mol Biol, 2005. **12**(6): p. 539-44.
69. Penczek, P.A., *Resolution measures in molecular electron microscopy.* Methods Enzymol, 2010. **482**: p. 73-100.
70. Laver, D.R., E.R. O'Neill, and G.D. Lamb, *Luminal Ca2+-regulated Mg2+ inhibition of skeletal RyRs reconstituted as isolated channels or coupled clusters.* J Gen Physiol, 2004. **124**(6): p. 741-58.
71. Lamb, G.D. and D.G. Stephenson, *Effect of Mg2+ on the control of Ca2+ release in skeletal muscle fibres of the toad.* J Physiol, 1991. **434**: p. 507-28.
72. Laver, D.R., T.M. Baynes, and A.F. Dulhunty, *Magnesium inhibition of ryanodine-receptor calcium channels: evidence for two independent mechanisms.* J Membr Biol, 1997. **156**(3): p. 213-29.
73. Meissner, G., *Adenine nucleotide stimulation of Ca2+-induced Ca2+ release in sarcoplasmic reticulum.* J Biol Chem, 1984. **259**(4): p. 2365-74.
74. Lanner, J.T., et al., *Ryanodine receptors: structure, expression, molecular details, and function in calcium release.* Cold Spring Harb Perspect Biol, 2010. **2**(11): p. a003996.
75. Meissner, G., E. Darling, and J. Eveleth, *Kinetics of rapid Ca2+ release by sarcoplasmic reticulum. Effects of Ca2+, Mg2+, and adenine nucleotides.* Biochemistry, 1986. **25**(1): p. 236-44.
76. Laver, D.R., G.K. Lenz, and G.D. Lamb, *Regulation of the calcium release channel from rabbit skeletal muscle by the nucleotides ATP, AMP, IMP and adenosine.* J Physiol, 2001. **537**(Pt 3): p. 763-78.
77. Samso, M., et al., *Coordinated movement of cytoplasmic and transmembrane domains of RyR1 upon gating.* PLoS Biol, 2009. **7**(4): p. e85.
78. Avila, G., et al., *FKBP12 binding to RyR1 modulates excitation-contraction coupling in mouse skeletal myotubes.* J Biol Chem, 2003. **278**(25): p. 22600-8.
79. Franzini-Armstrong, C. and F. Protasi, *Ryanodine receptors of striated muscles: a complex channel capable of multiple interactions.* Physiol Rev, 1997. **77**(3): p. 699-729.

80. Wong, P.W., W.R. Brackney, and I.N. Pessah, *Ortho-substituted polychlorinated biphenyls alter microsomal calcium transport by direct interaction with ryanodine receptors of mammalian brain.* J Biol Chem, 1997. **272**(24): p. 15145-53.
81. Wong, P.W. and I.N. Pessah, *Ortho-substituted polychlorinated biphenyls alter calcium regulation by a ryanodine receptor-mediated mechanism: structural specificity toward skeletal- and cardiac-type microsomal calcium release channels.* Mol Pharmacol, 1996. **49**(4): p. 740-51.
82. Pessah, I.N., R.A. Stambuk, and J.E. Casida, *Ca2+-activated ryanodine binding: mechanisms of sensitivity and intensity modulation by Mg2+, caffeine, and adenine nucleotides.* Mol Pharmacol, 1987. **31**(3): p. 232-8.
83. Henderson, R., *Avoiding the pitfalls of single particle cryo-electron microscopy: Einstein from noise.* Proc Natl Acad Sci U S A, 2013. **110**(45): p. 18037-41.
84. Shatsky, M., et al., *A method for the alignment of heterogeneous macromolecules from electron microscopy.* J Struct Biol, 2009. **166**(1): p. 67-78.
85. Scheres, S.H. and S. Chen, *Prevention of overfitting in cryo-EM structure determination.* Nat Methods, 2012. **9**(9): p. 853-4.
86. Grigorieff, N., *Resolution measurement in structures derived from single particles.* Acta Crystallogr D Biol Crystallogr, 2000. **56**(Pt 10): p. 1270-7.
87. Chen, S., et al., *High-resolution noise substitution to measure overfitting and validate resolution in 3D structure determination by single particle electron cryomicroscopy.* Ultramicroscopy, 2013. **135**: p. 24-35.
88. Brink, J., et al., *Experimental verification of conformational variation of human fatty acid synthase as predicted by normal mode analysis.* Structure, 2004. **12**(2): p. 185-91.
89. Leschziner, A.E. and E. Nogales, *Visualizing flexibility at molecular resolution: analysis of heterogeneity in single-particle electron microscopy reconstructions.* Annu Rev Biophys Biomol Struct, 2007. **36**: p. 43-62.
90. Orlova, E.V., et al., *Three-dimensional structure of low density lipoproteins by electron cryomicroscopy.* Proc Natl Acad Sci U S A, 1999. **96**(15): p. 8420-5.
91. Roseman, A.M., et al., *Structures of unliganded and ATP-bound states of the Escherichia coli chaperonin GroEL by cryoelectron microscopy.* J Struct Biol, 2001. **135**(2): p. 115-25.
92. Yang, S., et al., *Flexibility of the rings: structural asymmetry in the DnaB hexameric helicase.* J Mol Biol, 2002. **321**(5): p. 839-49.
93. Shatsky, M., et al., *Automated multi-model reconstruction from single-particle electron microscopy data.* J Struct Biol, 2010. **170**(1): p. 98-108.
94. Ludtke, S.J., et al., *The pore structure of the closed RyR1 channel.* Structure, 2005. **13**(8): p. 1203-11.
95. Kimlicka, L., et al., *Disease mutations in the ryanodine receptor N-terminal region couple to a mobile intersubunit interface.* Nat Commun, 2013. **4**: p. 1506.

96. Wriggers, W., R.A. Milligan, and J.A. McCammon, *Situs: A package for docking crystal structures into low-resolution maps from electron microscopy.* J Struct Biol, 1999. **125**(2-3): p. 185-95.
97. Serysheva, II, et al., *Structure of Ca2+ release channel at 14 A resolution.* J Mol Biol, 2005. **345**(3): p. 427-31.
98. McCarthy, T.V., K.A. Quane, and P.J. Lynch, *Ryanodine receptor mutations in malignant hyperthermia and central core disease.* Hum Mutat, 2000. **15**(5): p. 410-7.
99. Robinson, R.L., et al., *RYR1 mutations causing central core disease are associated with more severe malignant hyperthermia in vitro contracture test phenotypes.* Hum Mutat, 2002. **20**(2): p. 88-97.
100. Robinson, R., et al., *Mutations in RYR1 in malignant hyperthermia and central core disease.* Hum Mutat, 2006. **27**(10): p. 977-89.
101. Tung, C.C., et al., *The amino-terminal disease hotspot of ryanodine receptors forms a cytoplasmic vestibule.* Nature, 2010. **468**(7323): p. 585-8.

Vita

Joshua J Lobo was born on February 4 th 1989, in Mesaieed ,Qatar. He received his bachelor's degree in Electronics Engineering from Pune University, India in 2011.His capstone project in his undergraduate degree was "Cervical Cancer Detection in MATLAB Using Image Processing". It was here where he started and got his first introduction to the wide world of image processing and its varied applications. Due to his proclivity for Biology & Biotechnology he worked to unite his passions in an engineering context. This led him to pursue his Master's degree in Virginia Commonwealth University in 2012. His research interests include Image Processing applications in Biomedical contexts and Bioinformatics